

## Chapter 3

# A regional model of the Southern Ocean\*

From an oceanographic perspective, the Southern Ocean is probably the most challenging region to model. This challenge manifests itself in the relatively poor performance of many state-of-the-art ocean circulation models in the Southern Ocean. In this region, global climate models exhibit their largest biases and inter-model disagreements. Among these issues in the models are the representation of ocean water masses (Downes et al., 2010, 2011; Heuzé et al., 2013, 2015; Sallée et al., 2013b), ocean circulation (Meijers et al., 2012; Downes and Hogg, 2013; Farneti et al., 2015), surface ocean mixed layer (Sallée et al., 2013a), sea-ice cover (Turner et al., 2013; Mahlstein et al., 2013; Haumann et al., 2014), surface fluxes (Majkut et al., 2014; Frölicher et al., 2015; Kessler and Tjiputra, 2016), and atmospheric circulation (Swart and Fyfe, 2012; Bracegirdle et al., 2013; Hosking et al., 2013). These issues do not only occur in the simulated mean states, but are also pronounced in the models' simulated responses to changes in the climate system. Since the Southern Ocean plays a pivotal role in the climate system (chapter 1), the relatively large inter-model spread and biases induce large uncertainties in future projections and our understanding of past changes. To better understand the sensitivity of the Southern Ocean to changes in the climate system, I here intend to obtain a model that reproduces the present-day Southern Ocean's water mass structure and circulation as closely as possible and is constrained by fluxes at the boundaries (section 3.5). Nevertheless, biases will remain and have to be considered carefully (section 3.7). Changes in the climate system can then be imposed on the model by varying the boundary conditions (chapters 4 and 5).

In many respects the requirements for a model of the Southern Ocean region differ from the rest of the globe. One particular reason is its unique topographic setting without zonal boundaries, large meridional gradients, and relatively weak vertical gradients. This setting induces strong flows and high levels of baroclinic instabilities. Global climate models typically do not resolve the resulting meso-scale turbulent flow. More recently, eddy-resolving ocean components have

---

\*Parts of this chapter are part of a manuscript in preparation for Journal of Climate (see chapter 4)

been investigated in coupled global climate models (e.g. Dufour et al., 2015; Morrison et al., 2016) at a high computational cost. In order to reduce the computational cost, I will here apply a regional model described in section 3.1, with enhanced spatial resolution in higher latitudes (section 3.4). However, regional models have the challenge that they are influenced by the lateral boundary conditions, which have to be chosen and implemented carefully (section 3.5.5). Another major challenge stems from the generally weak or even inverted vertical gradients in temperature, salinity, and density in the Southern Ocean. They often violate a general assumption in ocean circulation models that horizontal motions are much larger than vertical motions and therefore fully rely on the parameterization of vertical processes rather than effectively solving the vertical equations of motion and transport (Griffies et al., 2000a). Such parameterizations of the surface and bottom boundary layers, as well as convective processes can hence induce large biases if they are not accurately adapted for the use in the Southern Ocean. They must be able to deal with a very large amplitude of the seasonal cycle that ranges between very stable conditions and shallow mixed layers in summer and marginally stable or unstable conditions and deep mixed layers in winter. I will discuss these issues in section 3.2.

Due to the weak stratification and the very thin isolating sea-ice layer that separates the cold atmosphere from the relatively warmer ocean, small inaccuracies in either the atmosphere, ocean, or sea ice can lead to strong amplifications of biases (e.g. Goosse et al., 1999; Goosse and Fichefet, 1999; Stössel et al., 2002, 2011, 2015; Timmermann and Beckmann, 2004; Mathiot et al., 2012; Kjellsson et al., 2015). Prescribing the surface fluxes rather than using a coupled model, can alleviate some of these problems (e.g. Treguier et al., 2010; Downes et al., 2015). Yet, the atmospheric fluxes are poorly constrained due to the limited availability of observational data especially in the sea-ice region (Speer et al., 2012; Bourassa et al., 2013), also leading to large biases in forced simulations. Biases induced by the forcing can be further reduced by an assimilation of ocean and sea-ice observational data (Mazloff et al., 2010; Cerovečki et al., 2011; Massonnet et al., 2013; Barth et al., 2015). In this study, I will use a novel approach and prescribe all surface fluxes, i.e. the atmospheric (section 3.5.1), sea-ice (section 3.5.2), and land-ice (section 3.5.3) forcing. This approach has the advantage of strongly constraining the model and, at the same time, enables to study the ocean response to changes in the prescribed forcing, which is the purpose of this thesis. However, it also implies that feedbacks in the system cannot be studied and that long-term changes are dependent on the forcing.

First, this chapter deals with the numerical representation of physical (sections 3.1, and 3.2) and biogeochemical (section 3.3) processes in the model. Then, I will describe the model domain, topography, and spatial grid (section 3.4), which is followed by a description of the forcing at surface and lateral boundaries (section 3.5) and by a description of model initialization, spin-up, and drift (section 3.6). Finally, I will provide a detailed evaluation of the model's mean state using observational data (section 3.7) and a summary of the current state of the model (section 3.8).

## 3.1 The Regional Ocean Modeling System (ROMS)

In this thesis, I model the Southern Ocean using the regional, forced, ocean circulation model ROMS (Regional Ocean Modeling System; Shchepetkin and McWilliams, 2003, 2005, 2009a). It numerically solves the set of primitive equations that describes the physics of the ocean (cf. Cushman-Roisin and Beckers, 2011), consisting of the mass and momentum budgets, the equation of state for seawater, and conservation equations for tracers such as temperature and salinity. These equations are discretized in an orthogonal, curvilinear coordinate system in the horizontal direction and a stretched, terrain-following coordinate system in the vertical direction (Song and Haidvogel, 1994; Shchepetkin and McWilliams, 2003, 2005).

ROMS originates from many previous advances in terrain-following models. Among the predecessors of ROMS (Shchepetkin and McWilliams, 2005) are the Princeton Ocean Model (POM; Blumberg and Mellor, 1987), the S-coordinate Primitive Equation Model (SPEM; Haidvogel et al., 1991; Haidvogel and Beckmann, 1999), and the S-Coordinates Rutgers University Model (SCRUM; Song and Haidvogel, 1994). Compared to these models, Shchepetkin and McWilliams (2005) advanced the mode-splitting and time-stepping (see also section 3.1.2). These advances allow for much larger time steps and thus ROMS is computationally much more efficient than its predecessors and can be used for larger scale, high-resolution applications.

There are multiple versions of ROMS that are supported by different institutes. The version that I am using in this thesis is the UCLA-ETH version and "ROMS" always refers to this version if not explicitly stated otherwise. This version includes most recent developments of the original UCLA version (Marchesiello et al., 2003; Shchepetkin and McWilliams, 2003, 2005, 2011; McWilliams et al., 2009; Lemarié et al., 2012b; Shchepetkin, 2015) as well as some complementary routines developed or coupled at ETH Zürich. The latter developments include the coupling of ROMS to biogeochemical-ecological models such as the nitrogen based Nutrient-Phytoplankton-Zooplankton-Detritus (NPZD) model (Gruber et al., 2006), and the Biological Elemental Cycling (BEC) model (Moore et al., 2004; Jin et al., 2008; Moore et al., 2013; Yang and Gruber, 2016, see section 3.3 for details). In this chapter, I will describe some further developments that are necessary to apply ROMS in the Southern Ocean (see sections 3.2, 3.5.2, 3.5.3, 3.5.1).

So far, ROMS has mostly been used to study coastal systems (e.g. Gruber et al., 2006, 2011; Lachkar and Gruber, 2011, 2013; Turi et al., 2014, 2016; Frischknecht et al., 2015). In the Southern Ocean, Byrne et al. (2014) applied ROMS in the South Atlantic region. This application showed that ROMS reproduces complex dynamical features of the Southern Ocean reasonably well. However, these simulations were only run on very short temporal and smaller spatial scales and are thus strongly controlled by the initial and boundary conditions. So, they essentially differ from the application in my thesis.

A number of studies have been carried out with the Rutgers version of ROMS (Shchepetkin and McWilliams, 2005; Haidvogel et al., 2008; Shchepetkin and McWilliams, 2009b) in the Southern Ocean by Dinniman et al. (2003, 2007, 2011, 2012). They showed that the model is able to reproduce a realistic circulation on the continental shelf regions in the Ross Sea (Dinniman et al., 2007, 2011) and the western side of the Antarctic Peninsula (Dinniman et al., 2011). Yet, these studies are very regional as well and confined to the shelf region. Some larger scale studies were carried out with the Bremerhaven Regional Ice Ocean Simulations model (BRIOS; Beckmann et al., 1999), which is a descendent of SPEM and therefore related to ROMS. BRIOS simulates a realistic water-mass structure and sea-ice cover in the Weddell (Beckmann et al., 1999; Timmermann et al., 2001; Schodlok et al., 2002) and Ross Seas (Assmann and Timmermann, 2005), providing reasonable grounds to believe that realistic large-scale applications in the Southern Ocean can be achieved with a terrain-following coordinate model.

### 3.1.1 Terrain-following coordinate system

The vertical coordinate system of ROMS is the pivotal difference to other commonly used ocean circulation models, i.e. z-level or isopycnal coordinates, and characterizes most of the advantages and disadvantages compared to these other models (Chassignet et al., 2000; Griffies et al., 2000a; Willebrand et al., 2001). Thus, in the following, I will first review the implications of using a terrain-following vertical coordinate system for modeling the Southern Ocean as a whole.

Terrain-following coordinate systems have historically been developed in ocean circulation models to study coastal regions. This is owing to their advantage of having an increasing vertical resolution as the water column shoals (Figure 3.2). In the high-latitude Southern Ocean, the high vertical resolution of the continental shelf waters and the natural representation of terrain-following, density-driven bottom flows allows, in principal, for a realistic production of AABW in such coordinate systems (Beckmann et al., 1999; Timmermann et al., 2001, 2002; Schodlok et al., 2002; Assmann and Timmermann, 2005; Rodehacke et al., 2007). In z-level models, i.e. in most global climate models, an accurate representation of AABW is a key issue. Often, they form only little or no AABW on the continental shelf or unrealistically produce AABW through open-ocean deep convection (Doney and Hecht, 2002; Heuzé et al., 2013), which leads to strong deviations in the Southern Ocean hydrography and circulation (Heuzé et al., 2013; Stössel et al., 2015). More recently, overflow parameterizations are developed to resolve such issues in z-level models (Chassignet et al., 2014; Snow et al., 2015). Isopycnal models only accurately represent AABW if the reference density is set deep enough (about 2000 m; Chassignet et al., 2003). As a consequence, models with terrain-following coordinates, such as ROMS, should in principle be ideal to study the formation of AABW and should provide an accurate representation of the deep-ocean water masses in the Southern Ocean, if a realistic surface forcing and surface mixing scheme were provided.

While having advantages that favor the representation of coastal regions and AABW formation in a terrain-following coordinate system, there are major disadvantages or challenges that have historically prevented the ocean modeling community from applying such models to large scales such as the deep-ocean basins and decadal to centennial time-scales (Barnier et al., 1998; Chassignet et al., 2000; Griffies et al., 2000a; Willebrand et al., 2001). The apparent challenges mostly arise from the stretching and tilting of the vertical coordinates as moving from the shallow coastal regions to the deeper ocean interior. These challenges, and approaches to mitigate them, have also been pointed out in a few existing basin-wide applications of ROMS in the Atlantic (Haidvogel et al., 2000) and the Pacific (Marchesiello et al., 2009; Lemarié et al., 2012b) and need consideration when modeling the Southern Ocean basin.

One major challenge is that, as the ocean gets deeper towards the interior basin, the vertical resolution in the surface ocean mixed layer decreases leading to a poorer representation of surface processes (Griffies et al., 2000a; Shchepetkin, 2005). In ROMS, this problem has partly been mitigated by introducing vertical stretching functions that enhance the resolution towards the surface and result in so-called vertical S-coordinates (Song and Haidvogel, 1994; Haidvogel and Beckmann, 1999; Haidvogel et al., 2000; Shchepetkin and McWilliams, 2003). An accurate representation of surface mixed layer processes in the Southern Ocean is sensitive to the vertical resolution at the surface and therefore to the choice of these stretching functions (see sections 3.4.2 and 3.7).

Several other challenges arise from the crossing of the terrain-following vertical coordinates with geopotential and isoneutral surfaces. On larger temporal and spatial scales, this interference can lead to numerical errors in the pressure gradients and the advection and diffusion of tracers. In small, regional domains this is less of a problem because water masses are renewed at the open boundary. However, in basin scale applications and over long-term integrations, as I attempt here, this effect can induce model drift and a degradation of the ocean interior water masses (Barnier et al., 1998; Marchesiello et al., 2009; Lemarié et al., 2012b). In ROMS, the pressure gradient errors have largely been mitigated by new numerical schemes (Shchepetkin and McWilliams, 2003). The second problem is that the crossing between vertical coordinate system with isoneutrals causes numerical, diapycnal mixing induced by higher order, diffusive tracer advection schemes, referred to as spurious mixing (Marchesiello et al., 2009). Such an advection scheme, i.e. a third-order upwind-biased advection scheme, is used in ROMS (Shchepetkin and McWilliams, 1998).

There are several ways one can mitigate spurious mixing to an acceptable level: One possible option is to reduce the angle between the vertical coordinates and the isoneutrals by smoothing of the topography with the drawback of losing realism. Another option is to increase resolution, which reduces errors associated with the finite differencing but increases the computational cost. A third option is to numerically split a hyperdiffusive part from the actual advection and rotate it in an isoneutral direction (Marchesiello et al., 2009; Lemarié et al., 2012b,a). The latter new

development is implemented in ROMS but requires more testing and is currently not compatible with the version I use in this thesis. Instead, I mitigate spurious mixing and pressure gradient errors by applying a more extensive topographic smoothing (section 3.4.3), and using a higher resolution than previous basin-scale applications (Marchesiello et al., 2009; Lemarié et al., 2012b, section 3.4.1). However, future efforts should be made to use the isoneutral advection scheme in this model setup and other basin-wide application of ROMS (Lemarié et al., 2012b).

In z-level models, numerical pressure gradient errors are not an issue as the isosurfaces of the model grid mostly align with geopotential surfaces. However, spurious diapycnal mixing can be problematic in z-level models (Griffies et al., 2000b), especially in higher latitudes due to the sloping isoneutrals in these regions, leading to a degradation of both AABW and AAIW in the interior ocean. A good representation of interior water masses in the Southern Ocean that is not influenced by spurious mixing can be obtained using isopycnal models (Hallberg and Gnanadesikan, 2006). However, their resolution decreases as stratification weakens, which is the disadvantage of using isopycnal models in the Southern Ocean.

### 3.1.2 Momentum & tracer equations

In the horizontal, the state variables in ROMS are staggered on an Arakawa-C grid. As a consequence, all tracers are situated in the center of the grid cell and the velocity components on the respective grid cell edges (Arakawa and Lamb, 1977; Haidvogel and Beckmann, 1999; Griffies et al., 2000a). The horizontal momentum equations in ROMS are solved in a split-explicit time-stepping scheme (Shchepetkin and McWilliams, 2005, 2009a), which separates the faster barotropic mode from the slower baroclinic mode. Thus, the model calculates the evolution of the depth-integrated flow, i.e. the barotropic mode, at a much faster time step (here chosen as 70 times the slow time step) than the vertical deviations from the barotropic flow, i.e. the baroclinic mode, and all other processes. The baroclinic momentum and tracer equations are advanced in time using a leap-frog predictor sub-step followed by a third-order accuracy Adams-Moulton corrector sub-step. Mode coupling only occurs for the corrector sub-step (Shchepetkin and McWilliams, 2005, 2009a).

ROMS has a free surface (Shchepetkin and McWilliams, 2005); hence it is able to resolve the evolution of the surface elevation and the barotropic gravity waves, which are about two orders of magnitude faster than the baroclinic waves (Griffies et al., 2000a). This approach has several advantages over the rigid-lid and implicit free-surface methods (Killworth et al., 1991; Griffies et al., 2000a; Shchepetkin and McWilliams, 2005): Among these are a better numerical stability and flow characteristics over rough topography, a straightforward implementation of the input of freshwater, and computational efficiency.

The formulation of the vertical momentum equation assumes hydrostatic balance (cf. Cushman-

Roisin and Beckers, 2011). Even though the hydrostatic approximation is commonly used in ocean circulation models, it is clearly a disadvantage in applications in the Southern Ocean. Here, due to the low static stability, the water-mass structure and circulation are sensitive to vertical motions like coastal (Jacobs et al., 1985; Ohshima et al., 2013; Gordon et al., 2015) and open-ocean convection (Gordon, 1991; Martinson, 1991; Marshall and Schott, 1999) or small-scale salt plumes from the formation of sea ice (Duffy and Caldeira, 1997; Duffy et al., 1999; Nguyen et al., 2009). All these processes should ideally be represented in a model of the Southern Ocean and have to be parameterized in a hydrostatic model (cf. section 3.2).

Kanarska et al. (2007) developed a non-hydrostatic version of ROMS. However, this version is computationally more expensive and requires a much higher vertical resolution. Additionally, it has not yet been extensively validated in realistic oceanographic studies and many additional numerical challenges arise from the implementation that might introduce new numerical errors. Consequently, I am not yet able to apply this non-hydrostatic version to a basin-wide study of the Southern Ocean.

### 3.1.3 Equation of state

As most models in geophysical fluid dynamics, ROMS makes use of the Boussinesq approximation, which states that deviations of density around a reference density  $\rho_0$  (here I chose  $\rho_0 = 1027 \text{ kg m}^{-3}$ ) are small (cf. Cushman-Roisin and Beckers, 2011). This approximation entails the assumption of sea-water incompressibility. Yet, there is an exception implemented in ROMS to reduce errors in the mode splitting due to the Boussinesq approximation. This correction is done by accounting for the compression induced by vertical pressure changes in the barotropic mode (option “SPLIT\_EOS”; Shchepetkin and McWilliams, 2009a, 2011). Consequently, ROMS provides an intermediate solution of using all the numerical advantages resulting from the Boussinesq approximation and correcting for the major errors associated with this assumption (Dukowicz, 2001). Despite these simplifications of density effects, ROMS calculates the full, non-linear equation of state (Jackett and McDougall, 1995; Shchepetkin and McWilliams, 2003, 2011). It should be noted that this version does not correspond to the newest formulation of the equation of state (TEOS10, IOC, SCOR, and IAPSO, 2010). The resulting *in situ* density enters the calculation of the pressure gradient, the barotropic mode, the static stability, the surface buoyancy forcing (Shchepetkin and McWilliams, 2011), and the double diffusion (Large et al., 1994).

Particularly important to my study is an accurate representation of the equation of state in the calculation of the static stability (see section 1.3.2). Several stability effects result from the non-linearity of the equation of state in the Southern Ocean: Firstly, the density stratification is much more sensitive to salinity changes at low temperatures (Sigman et al., 2004; de Boer et al., 2007). Secondly, non-linearity effects like thermobaricity and cabbeling are important factors for water-mass transformation (McDougall, 1987; Stewart et al., 2016). McPhee (2003) argues that

thermobaricity, i.e. the pressure dependence of the thermal expansion coefficient, might be an important trigger for convective events in the the Southern Ocean. Cabbeling, i.e. the mixing of two water parcels of the same density but with different temperature and salinity and a heavier resulting density, is thought to be an important factor for the formation of AAIW and SAMW (Iudicone et al., 2008; Urakawa and Hasumi, 2012). However, whether or not such effects are accurately represented in ROMS does not only depend on the formulation of the equation of state in the model but also on the formulation of mixing and convective processes (McDougall, 1987; Ilicak et al., 2012). Nevertheless, a future update of the equation of state to the newest and most accurate formulation (TEOS10, IOC, SCOR, and IAPSO, 2010) might improve the representation of water masses in the model.

## 3.2 Mixing processes

Numerical models of the ocean generally resolve the ocean circulation and variations of properties on large temporal and spatial scales. Processes that cannot be resolved in these models are often parameterized. The most critical unresolved processes are sub-grid-scale turbulence occurring in the vertical (sections 3.2.2 and 3.2.1) and horizontal (section 3.2.3), as well as vertical convection due to static instabilities. Other commonly parameterized mixing processes are double diffusion or internal wave breaking (section 3.2.1). In ROMS, vertical mixing processes are parameterized through  $K$ -theory (cf. Stull, 1988). This first-order closure scheme suggested by Large et al. (1994) approximates mixing processes through the product of the vertical gradient of momentum and tracers and the corresponding local eddy viscosity and diffusivity coefficients. Eddy diffusivity coefficients are calculated separately for temperature and for salt and all other tracers. This mixing scheme treats the oceanic surface and bottom boundary layer (section 3.2.2) and mixing in the ocean interior (section 3.2.1) separately.

As my thesis focuses on the relation between stratification and vertical exchange of tracers, an accurate representation of processes associated with mixing are critical. On the one hand, they determine the exchange of tracers such as carbon and nutrients between the surface and subsurface ocean (Gargett, 1991; Bopp et al., 2015). On the other hand, mixing processes determine the transformation of water masses in the Southern Ocean, i.e. the upwelling of CDW and the subduction of AABW, AAIW, and SAMW, and consequently the ventilation of the subsurface ocean (Orsi et al., 1999; Sloyan and Rintoul, 2001a; Jacobs, 2004; Iudicone et al., 2008; Urakawa and Hasumi, 2012). Consequently, it is an important contributor to the overturning circulation (Sloyan and Rintoul, 2001b; Lumpkin and Speer, 2007; Ito and Marshall, 2008; Marshall and Speer, 2012). Surface and subsurface mixing processes are also essential for setting up the typical hydrographic structure with its pronounced halocline, which is determined by a subtle balance between the surface buoyancy fluxes and vertical mixing and advection processes at the bottom of the surface mixed layer (Gordon and Huber, 1984; Gordon, 1991; Martinson, 1990, 1991, see also section 1.3.2). This important role that mixing plays for the vertical exchange in the Southern Ocean mostly stems from the combination of a low static stability with strong turbulent shear and wind-driven stirring.

### 3.2.1 Vertical interior ocean mixing

ROMS first calculates the vertical eddy viscosity and diffusivity for the entire water column in absence of the surface and bottom boundary layers. Following Large et al. (1994), these values are the sum of the corresponding contributions from turbulent shear, convection, double diffusion, and internal wave breaking. The latter dominates the kinetic energy spectrum at very small scales in the interior ocean (Wunsch and Ferrari, 2004; Ferrari and Wunsch, 2009; Nikurashin

et al., 2012) and is parameterized in ROMS as suggested by Large et al. (1994) with a constant background vertical viscosity of  $10^{-4} \text{ m}^2 \text{ s}^{-1}$  and diffusivity of  $10^{-5} \text{ m}^2 \text{ s}^{-1}$ . Turbulent mixing due to shear instabilities in the vertical velocity profile is much larger than the mixing by internal waves, but it is typically regionally and temporally confined to regions of strong currents and in close proximity to boundaries. In ROMS, the associated diffusivity is computed from the ratio of the local gradient Richardson number and a critical value  $Ri_0$  of 0.7. The latter is an empirical value at which local destabilizing shear tends to dominate over stabilizing density stratification:

$$\hat{Ri}_g = \frac{1}{Ri_0} \cdot \frac{N^2}{(\partial u / \partial z)^2 + (\partial v / \partial z)^2}. \quad (3.1)$$

In this formulation, values of  $\hat{Ri}_g$  larger than 1 are associated with a stable stratification that suppresses shear instabilities and ROMS sets  $\hat{Ri}_g$  to an exact value of 1. If  $\hat{Ri}_g$  drops below 0,  $N^2$  must be negative and therefore the stratification must be unstable. In this case ROMS sets  $\hat{Ri}_g$  to an exact value of 0. Using this ratio and a maximal diffusivity  $\nu_0$ , the resulting diffusivity due to the turbulent shear  $\nu$  is (see Large et al., 1994)

$$\nu = \nu_0 \cdot \left(1 - \hat{Ri}_g^2\right)^3. \quad (3.2)$$

Therefore,  $\nu$  is 0 if no shear instability occurs and increases towards  $\nu_0$  as either stratification weakens or the vertical velocity gradient strengthens. Large et al. (1994) suggest a value of  $0.005 \text{ m}^2 \text{ s}^{-1}$  for  $\nu_0$ , which is used in most standard applications of ROMS. I found that this value can change the representation of the water-mass structure in ROMS in the Southern Ocean and that a larger value of  $0.01 \text{ m}^2 \text{ s}^{-1}$ , which I will use here, is more suitable. The main motivation for increasing the shear-induced diffusivity is an observed layer of increased diffusivity in the ACC region under the actual mixed layer (Forryan et al., 2015; Nicholson et al., 2016).

Due to the low static stability of the interior Southern Ocean, deep ocean convection is a process that can occur (Gordon, 1991). Therefore, and as a consequence of the hydrostatic approximation (section 3.1.2), convective processes due to local static instabilities should be parameterized in this model as well. The above equation 3.2 has the advantage that static instabilities are automatically accounted for because  $\nu$  reaches its maximum value of  $\nu_0$ . As long as  $\nu_0$  takes a sufficiently large finite value an additional parameterization of convective processes is not required. I therefore switched the C-preprocessing option (CPP-switch) *LMD\_CONVEC* off. The value of  $\nu_0$  that is added to the overall diffusivity in case of static instabilities is somewhat smaller than the ROMS standard value of  $0.1 \text{ m}^2 \text{ s}^{-1}$  in the *LMD\_CONVEC* routine, but it corresponds to the value suggested by e.g. Timmermann and Beckmann (2004) for the Southern Ocean. Griffies et al. (2000a) argue that such an approach of enhancing the local diffusivity is physically more realistic and numerically more appropriate than classical convective adjustment approaches, which mix vertical grid boxes iteratively or add an infinitely large vertical diffusivity.

Molecular diffusion is typically several orders of magnitudes smaller than turbulent and con-

vective mixing processes and hence neglected in most ocean circulation models. Nevertheless, one exception to that is double diffusion, which results from the fact that heat diffuses more rapidly than salt leading to convective mixing (Turner, 1973). Regionally and locally, such processes can be important for the vertical exchange of nutrients to the surface (Oschlies et al., 2003). Zhang et al. (1998) even suggest that double diffusion could ultimately be important on a global scale through its effects on mixing of water masses and the overturning circulation. In the upper Southern Ocean, where cold and fresh water overlies warm and salty water, double diffusion can occur in the form of diffusive convection and numerous studies suggested that it contributes to the upper ocean water-mass structure (Middleton and Foster, 1980; Muench et al., 1990; Martinson, 1990). The opposite, i.e. salt-fingering, might occur at depth where warm and salty NADW overlies the colder and fresher AABW. In order to account for these processes, I will use a double diffusion parameterization implemented in the vertical mixing scheme of ROMS (Large et al., 1994; Marmorino and Caldwell, 1976). ROMS computes salt and temperature diffusivities that result from double diffusion as a function of the local density ratio. These diffusivities are added to the overall vertical diffusivity coefficients of each tracer at each grid point.

### 3.2.2 Boundary layer mixing

Models of the surface ocean boundary layer are typically formulated either in a bulk or continuous mixed layer scheme (Griffies et al., 2000a). The  $K$ -profile parameterization (KPP; Large et al., 1994; Shchepetkin, 2005; McWilliams et al., 2009) in ROMS is of the latter type. Consequently, it allows for a vertical structure of tracers and velocity over the mixed layer extent as compared to the uniform distribution in the bulk method (Griffies et al., 2000a). KPP first computes the local vertical acceleration  $a_c$  from shear, buoyancy, rotation, and turbulent entrainment according to (Shchepetkin, 2005; McWilliams et al., 2009):

$$a_c(z) = \int_z^0 \frac{|z|}{|z| + \epsilon h_{bl0}} \left[ \underbrace{\left( \frac{\partial \vec{u}(z)}{\partial z} \right)^2}_{\text{shear}} - \underbrace{\frac{N(z)^2}{Ri_c}}_{\text{buoyancy}} - \underbrace{C_{Ek} f^2}_{\text{rotation}} \right] dz + \underbrace{C_{ent} N(z) w_s}_{\text{entrainment}} . \quad (3.3)$$

Here,  $z$  is the height of the layer (negative downward),  $h_{bl0}$  is an initial guess of the depth of the mixed layer (usually the previous time step),  $\vec{u}$  is the horizontal velocity vector,  $N$  is the buoyancy frequency,  $f$  is the Coriolis parameter, and  $w_s$  is the turbulent velocity scale that depends on the surface forcing. The depth of the mixed layer ( $h_{bl}$ ) corresponds to the first level below the surface at which  $a_c(z) = 0$ . This is a modification (Shchepetkin, 2005; McWilliams et al., 2009) of the original bulk Richardson number formulation in KPP (Large et al., 1994) that essentially allows to diagnose separate contributions to vertical mixing. Subsequently, KPP fits a vertical profile of diffusivity through the boundary layer using a non-dimensional vertical shape function (Large et al., 1994) and therefore gives the boundary layer a vertical structure

that continuously transitions into the ocean interior with a value of 0 at the bottom of the surface boundary layer. The non-dimensional profile is then multiplied with the boundary layer depth and the turbulent velocity scale to get a value for the local diffusivity. This diffusivity is added to the background diffusivity (section 3.2.1). Additionally, KPP calculates a non-local transport term that accounts for the unresolved penetration into the layers below the mixed layer.

The separation of buoyancy and turbulent mixing effects, as well as the first-order turbulent closure technique in KPP, make it generally applicable to any region in the global ocean and under a variety of conditions. Therefore, KPP has become widely used in ocean models (Griffies et al., 2000a). Most models produce too shallow mixed layers in the Southern Ocean, especially in summer (Sallée et al., 2013a; Downes et al., 2015). Such a shallow bias, especially in the melting season of the sea ice, is a well-known bias in KPP (Dinniman et al., 2003, 2011; Timmermann and Beckmann, 2004; Li et al., 2016). This shallow bias during summer promotes in some extreme cases deep ocean convection in winter as the thin surface layer becomes statically unstable. In many respects this bias leads to large biases in the water-mass structure in both higher and lower latitudes as well as biases in the overturning circulation. Initial simulations with ROMS showed a very similar behavior with a strongly underestimated mixed layer depth (Eberenz, 2015), leading to a long-term degradation of AAIW and a too fresh surface layer. Sallée et al. (2013a) interpreted this too fresh surface ocean associated with the shallow mixed layer bias in the global models as a too strong surface freshwater forcing. Based on sensitivity tests with ROMS that I performed for this thesis, I argue that such an overly-fresh surface ocean in global models might also be related to a reduced mixing of freshwater into the deeper layers, leading to a generally salty bias in AAIW if mixed layers are too shallow. This is a critical process with respect to the amount of AAIW formed and the subduction of heat and carbon with these waters (Frölicher et al., 2015). Consequently, the shallow mixed layer bias in global models and the general tendency to take up less carbon than suggested by inverse models might be directly related (Khatiwala et al., 2013; Mikaloff Fletcher et al., 2006; Frölicher et al., 2015).

In ROMS, the overly-shallow summer-time mixed layer is associated with a very fast stabilization of the surface ocean as the sea ice melts and the surface ocean heats up. In extreme cases, the surface mixed layer continuously shoals until it only consists of half of the upper most grid cell and diffusivities drop to the background minimum. Therefore, the surface mixed layer was effectively absent in these cases. Such a run away process is critical because KPP is not able to properly fit a vertical profile if only one or two grid points are available. Increasing the vertical resolution, I found that the mixed layer deepens and that run away effects can be avoided because KPP has more grid points to fit a vertical profile. This effect is especially critical if KPP is used in combination with a terrain-following model in the deep ocean and vertical grid parameters have to be chosen carefully (see section 3.4.2). I further added a constraint to the model that the mixed layer diffusivity is always computed as described above for the interface between the first and the second layer, even if the mixing depth drops below the depth of the uppermost layer (CPP-switch *LMD\_MIN\_KPP*). A further deepening of the mixed layer occurs with an increase

in horizontal resolution (section 3.7). The computation of  $h_{bl}$  through equation 3.3 does not give many possibilities for further modifications, except for the entrainment term, which is not well constrained and could be used for further tuning (Danabasoglu et al., 2006). Additional improvements have been obtained in other studies by implementing mixing through surface waves (Huang et al., 2012; Qiao and Huang, 2012; Li et al., 2016), which is currently not included in ROMS and could significantly deepen the mixed layer in the Southern Ocean. Timmermann and Beckmann (2004) also suggest to parameterize keel stirring by sea ice as a function of ice drift velocity. The latter two processes would be highly desirable in future versions of ROMS.

While all the above suggestions lead to slight improvements, none of them seems to ultimately resolve the shallow bias and the insufficient subsurface mixing south of the frontal zone during summer. The key problem that I identified here as a cause of the shallow mixing during summer is not the mixing intensity, i.e. the diffusivity itself, or the critical depth that the mixing reaches, but rather a too quick shoaling of the mixed layer under stable conditions if the surface momentum stress decreases. Niiler and Kraus (1977), Lemke (1987), and Markus (1999) argue that the mixing depth  $h_{bl}$  for such a thinning mixed layer can be diagnosed through the ratio between the friction velocity  $u^{*3}$  and the surface buoyancy forcing  $B_0$ , which is the Monin-Obukhov length scale, and an exponential dissipation function. Both Timmermann and Beckmann (2004) and Dinniman et al. (2003, 2011) use this relation to adjust the vertical diffusivity in their respective continuous mixing schemes when the surface boundary layer shoals, following the suggestions by Lemke (1987) and Markus (1999). I here use a similar approach and recalculate the mixed layer depth when mixed layer thins through:

$$\hat{h}_{bl} = \frac{u^{*3}}{B_0 \kappa} e^{-h_{bl0}/h_0} . \quad (3.4)$$

Here,  $\kappa$  is the *von Karman* constant (0.41),  $h_{bl0}$  is an initial estimate of the mixed layer depth, which is here provided through the mixed layer depth of the previous time step, and  $h_0$  is the dissipation length scale set to 20 m (Lemke, 1987; Markus, 1999). Hereafter, the calculation of the diffusivity throughout the adjusted mixed layer depth is performed in the normal way using the KPP shape function. This adjustment provides reasonable solutions of the mixed layer depth and is key to obtaining a better hydrography. The disadvantage of this formulation is that it overwrites the mixed layer depth calculated through equation 3.3 for thinning mixed layers. A potentially more ideal solution would be to dampen the decay of deep mixed layers under stabilizing conditions in time. Such a solution would be consistent with several observational and modeling studies that suggest that storms and eddies in the Southern Ocean induce strong inertial motions and shear induced mixing in the upper ocean that last for multiple days to weeks (Zhai et al., 2005; Brannigan et al., 2013; Meyer et al., 2015; Merrifield et al., 2016; Nicholson et al., 2016). Nicholson et al. (2016) recently suggested that this process might lead to the observed enhanced diffusivity in the subsurface layer in the Southern Ocean during summer. Given that this issue is the most critical to obtain a reasonable simulation and that many global models seem

to suffer from similar issues, it is an urgent matter to further investigate potential solutions in future.

Another surface mixing process is the development of convective salty plumes from the rejection of salty brine to the ocean when sea ice forms during winter. This process is spatially heterogeneous and typically happens on scales from centimeters to kilometers (Nguyen et al., 2009). Local static instabilities can occur in the water column below the sea ice leading to salt plume convection on horizontal scales that are much smaller than what is resolved by the model or the forcing. If shear induced turbulent mixing is small (Barthélemy et al., 2015), these plumes sink until they reach a neutrally buoyant depth, which is typically the halocline. If in the model the brine was added to the top layer, it would make the surface layers much saltier until a static instability and convective mixing occurs over the entire grid cell and for all tracers. In models such a process can lead to unrealistically deep winter-time mixed layers and an erosion of the halocline. In some cases, such elevated surface salinities can even lead to spurious deep convection in global climate models (Duffy and Caldeira, 1997; Duffy et al., 1999). Considering several studies that have investigated the effect of sub-grid scale brine rejection parameterizations (Duffy and Caldeira, 1997; Duffy et al., 1999; Nguyen et al., 2009; Barthélemy et al., 2015) and running some sensitivity experiments with ROMS, I conclude that the effect of a brine rejection parameterization is largely dependent on the model and the associated surface mixed layer parameters. I implemented a simplified version according to Duffy et al. (1999, CPP-switch *BRINE PLUMES*) that distributes the salt flux from the sea-ice formation equally over the surface boundary layer calculated by KPP. I will here use this parameterization as it improves the representation of the surface mixed layer and surface heat fluxes in the sea-ice region. If this parameterization is not used, the winter-time heat loss from the surface ocean is unrealistically high and some local deep convection occurs.

The water-mass structure in the Southern Ocean is generally very sensitive to the surface mixed layer, especially in the sea-ice region (Goosse and Fichefet, 1999; Goosse et al., 1999; Stössel et al., 2002). A better representation of the mixed layer can usually be achieved by either adapting the surface forcing or tuning the mixed layer scheme (Kjellsson et al., 2015). Additional to the modifications of KPP and its parameters that I described in this section, an accurate treatment of the ice-ocean surface fluxes turned out to be critical for obtaining a realistic surface mixed layer (see section 3.5.2).

Additional to the surface boundary layer, I will also use the bottom boundary layer option of KPP in this thesis, which is computed in the same way as the surface boundary layer. I chose a bottom roughness length of 0.02 m, which is slightly higher than the value used originally (0.01 m). The reason for enhancing the bottom roughness length is to counteract the effects induced by smoothing the topography (see section 3.4.3). This modification helped to slow down an overly-fast coastal current around Antarctica.

### 3.2.3 Lateral mixing

A dominant fraction of the turbulent kinetic energy in the ocean is contained in the mesoscale, which spans from tens to a hundred kilometers (Ferrari and Wunsch, 2009; Nikurashin et al., 2012). A large portion of this energy is situated in the form of geostrophic eddies in regions of strong currents and high baroclinicity, such as the ACC, the Brazil-Malvinas confluence zone, or the Agulhas Current System (Wunsch and Stammer, 1998; Frenger et al., 2015). It is hence important to account for this mesoscale turbulence in model simulations especially in the Southern Ocean, where it contributes to both the lateral and overturning circulation (Hallberg and Gnanadesikan, 2001, 2006; Henning and Vallis, 2005; Sallée et al., 2011; Meredith et al., 2012; Morrison and Hogg, 2013).

In coarse resolution models, which do not resolve the mesoscale, lateral mixing is typically parameterized. However, simply mixing along horizontal surfaces would lead to spurious diapycnal mixing in regions of sloping isopycnals, such as the ACC region. Thus, an isopycnal mixing scheme has been implemented in most ocean circulation models to account for mesoscale eddy fluxes (Gent and McWilliams, 1990; Gent et al., 1995; Farneti and Gent, 2011). High-resolution simulations showed that a certain degree of horizontal adiabatic diffusion is still required, even if most of the mesoscale processes are resolved to ensure numerical stability (Roberts and Marshall, 1998). For this reason, resolution-dependent eddy parameterizations have been developed (Gent et al., 2002; Smith and Gent, 2004). However, no such parameterizations are implemented in ROMS. Instead the advection scheme in ROMS contains a resolution-dependent hyperdiffusion, as described in section 3.1.1, to ensure numerical stability (Shchepetkin and McWilliams, 1998). This diffusion operator vanishes as the resolution increases. Additionally, ROMS provides the possibility for harmonic (Laplacian) mixing through constant viscosity and diffusivity coefficients, which I will not use in this thesis. I here intend to resolve most of the mesoscale processes in the Southern Ocean (see section 3.4.1).

### 3.3 Biogeochemical-ecological component

In chapter 5, I will analyse the response of the Southern Ocean carbon fluxes to changes in surface freshwater fluxes and stratification. For this purpose, I will run simulations with a coupled biogeochemical and ecological component. ROMS has two optional biogeochemical-ecological sub-models: A nitrogen based Nutrient-Phytoplankton-Zooplankton-Detritus (NPZD) model (Gruber et al., 2006) and the Biological Elemental Cycling (BEC) model (Moore et al., 2001b, 2004). Even though it is computationally more expensive due to a larger number of tracers, BEC is the obvious choice for simulations in the Southern Ocean because it includes iron limitation (Moore et al., 2001a).

BEC explicitly simulates the cycling of carbon, major nutrients (nitrate, ammonium, phosphate, dissolved iron, and silicate), dissolved oxygen, and alkalinity in the ocean (Moore et al., 2001b, 2004). The carbon cycle includes dissolved organic and inorganic carbon (DOC, DIC) pools, as well as the sinking of particulate organic matter (POM). The model has one prognostic zooplankton type and three prognostic phytoplankton groups, i.e. small phytoplankton, diatoms, and diazotrophs. Coccolithophores and the production of calcium carbonate ( $\text{CaCO}_3$ ) are so far implicitly represented as a fraction of small phytoplankton. The development of an explicit coccolithophore group is currently underway at ETH Zürich (Ph.D. project by C. Nissen). All phytoplankton growth rates include limitations by several nutrients, temperature, and light. Zooplankton grazing on the phytoplankton is concentration-dependent. Next to the environmental forcing from the physical model, BEC is forced with atmospheric partial pressure of  $\text{CO}_2$ , and dust and iron deposition at the surface (see section 3.5).

BEC was originally developed as part of the Community Earth System Model (CESM) at the National Center for Atmospheric Research (Moore et al., 2001b, 2004). Jin et al. (2008) previously used BEC coupled to ROMS for simulations in the Pacific. The version that I will be using in this thesis includes all most recent developments such as a better representation of the sinks and sources of nutrients (Moore et al., 2013; Yang and Gruber, 2016). The computational expenses increase by roughly a factor three to four when running ROMS coupled with BEC. Next to the additional prognostic variables, the writing of numerous diagnostic variables required for example for the analysis of the carbon budget significantly increase the computational and post-processing efforts. Therefore, I will be running the coupled model only at a nominal resolution of  $0.5^\circ$  degrees, which should be improved in future efforts.

## 3.4 Model setup

For the purpose of this thesis, I developed a new ROMS setup that covers the entire Southern Ocean (Figure 3.3). Multiple aspects in this setup differ from applications of ROMS in other regions. In the meridional direction the setup extends from 24° S to about 78.8° S, with the latter exact value depending on the chosen horizontal resolution (see Table 3.1). This choice of the northern boundary has the advantage that most coastlines and ocean currents (center of the subtropical gyres) are oriented perpendicular to the boundary and therefore ensure a more stable model with less problematic boundary artifacts. The condition for the southern boundary was to include the entire Antarctic coastline and thereby creating a closed southern boundary for the model. In the zonal direction, the domain is east-west periodic (CPP-switch *EW\_PERIODIC*) with an exchange between the eastern and western boundary at 24° E ( $\lambda_0$ ). I chose this longitude over the center of the African continent in order not to interrupt the northern boundary in one of the ocean basins, which would be problematic for the northern boundary condition (section 3.5.5). The only open boundary is therefore the northern boundary (CPP-switch *OBC\_NORTH*), which is divided into the three major ocean basins. I had to implement some adjustments to the open boundary condition in the north that are specific to this setup as I will describe in detail in section 3.5.5. In this section, I will continue to describe the different horizontal resolutions at which the setup is available, the vertical grid, the topography, and the land-sea-ice mask.

### 3.4.1 Horizontal grid & resolution

I here use a stretched longitude-latitude, staggered coordinate system in the horizontal. The model grid follows longitudes ( $\lambda$ ) in the  $\xi$ -direction (x-direction) at a regular spacing. The grid cell center ( $\rho$ -points) in the  $\xi$ -direction is defined through:

$$\lambda_\rho(\xi) = \lambda_0 - \frac{\delta_\lambda}{2} + \xi \cdot \delta_\lambda . \quad (3.5)$$

Here,  $\delta_\lambda$  denotes the spacing in degrees longitude in the  $\xi$ -direction. In the  $\eta$ -direction (y-direction), the model grid follows latitudes ( $\phi$ ) but the spacing is irregular. For each latitude band, I calculated the absolute distance between two  $\lambda_\rho$  points and applied this distance as spacing in  $\eta$ -direction. Therefore, each grid box has approximately the same size in  $\xi$ - and  $\eta$ -direction. The position of the grid point center is determined in two iterative steps from north to south:

$$\phi_\rho(\eta) = \phi_\rho(\eta + 1) - \delta_\lambda \cdot \cos \left( \phi_\rho(\eta + 1) \cdot \frac{\pi}{180} \right) , \quad (3.6)$$

$$\phi_\rho(\eta) = \phi_\rho(\eta + 1) - 0.5 \cdot \delta_\lambda \cdot \cos \left( \phi_\rho(\eta + 1) \cdot \frac{\pi}{180} \right) - 0.5 \cdot \delta_\lambda \cdot \cos \left( \phi_\rho(\eta) \cdot \frac{\pi}{180} \right) . \quad (3.7)$$

After defining the horizontal grid, I used the standard *ROMSTOOLS* to create a grid-file that is used by the model and contains all necessary information.

**Table 3.1 Model domain extent, resolution, and tiling of Southern Ocean ROMS setup.**

$\delta_\lambda$ [° E]	$\delta_{south}$ [km]	$\delta_{north}$ [km]	$\phi_{south,\rho}$ [° N]	$\phi_{north,\rho}$ [° N]	$\lambda_{east,\rho}$ [° E]	$\lambda_{west,\rho}$ [° E]	$n_\eta$ [-]	$n_\xi$ [-]	$p_\eta$ [-]	$p_\xi$ [-]
1/2	10.7664	50.6087	-78.8826	-24.2280	23.7500	384.2500	218	722	36	8
1/4	5.4062	25.3501	-78.8102	-24.1141	23.8750	384.1250	434	1442	36	16
1/8	2.7089	12.6864	-78.7738	-24.0571	23.9375	384.0625	866	2882	24	32
1/10	2.168	10.1509	-78.7665	-24.0457	23.9500	384.0500	1082	3602	24	40

$\phi$  denotes the latitude,  $\lambda$  the longitude,  $\delta_\lambda$  the resolution in the zonal direction,  $\delta_{south}$  and  $\delta_{north}$  the spatial resolution at the southern and northern boundaries,  $n$  the number of grid points,  $p$  the recommended number of partitions,  $\eta$  the meridional- or y-direction,  $\xi$  the zonal- or x-direction. Numbers include ghost-points on either side of the domain.

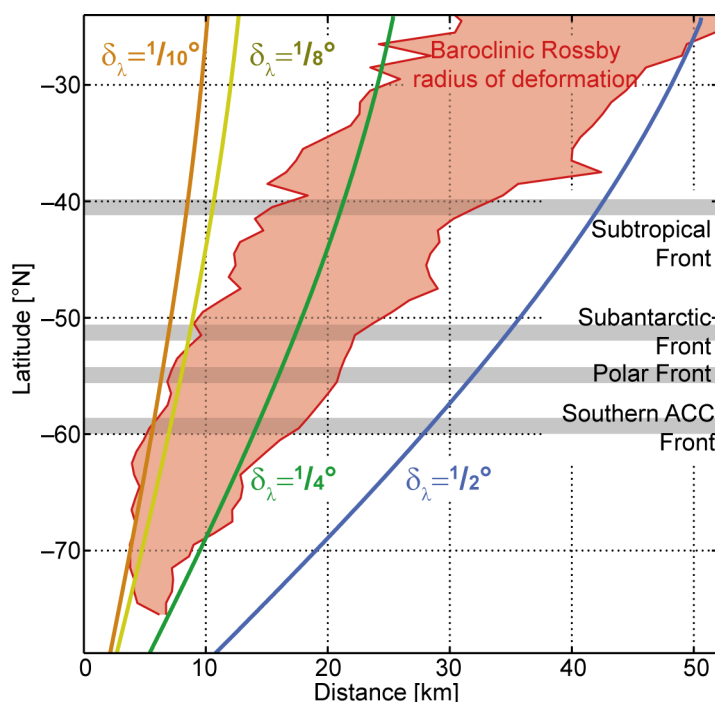


**Figure 3.1 Variation of different model resolutions with latitude:** Colored lines show the variation of the spatial resolution with the respective zonal resolution in degrees longitude as in Table 3.1. The red area spans the minimum and maximum baroclinic Rossby radius of deformation at each latitude from Chelton et al. (1998). The location of the fronts (gray) is the circumpolar mean of the fronts from Orsi et al. (1995).

ROMS requires so-called ghost points that are added on either boundary (one row or column each). In this setup, these ghost points exchange information from one side of the domain to the other in the east-west direction (CPP-switch *EW\_PERIODIC*). The grid corner points and number of grid points in either direction including the ghost points are listed in Table 3.1 for four different possible resolutions. Note that this spatial resolution  $\delta_\lambda$  only indicates the zonal resolution, since the actual resolution depends on the latitude. Such a grid has the advantage of naturally converging longitudes towards the pole and therefore a refinement of the spatial resolution towards the south. This stretching of the grid gives a considerable computational advantage. At the same time, it has a higher resolution where the eddy activity is high in the ACC region (Frenger et al., 2015) and follows the natural decrease of the baroclinic Rossby radius of deformation towards

the pole (Figure 3.1), which sets the length scale for baroclinic instabilities in the ocean (Chelton et al., 1998; Hallberg, 2013).

The coarsest resolution of  $0.5^\circ$  longitude ranges between about 50 km at the northern boundary and about 10 km at the Antarctic coast (Figure 3.1). In the ACC region, this grid has a resolution of about 30 km, which already allows to resolve some meso-scale eddies that have an average diameter of about 80 km (Frenger et al., 2013). The  $0.25^\circ$  longitude resolution closely follows the baroclinic Rossby radius of deformation (Chelton et al., 1998) and therefore permits for some meso-scale activity. The  $0.125^\circ$  and  $0.1^\circ$  longitude resolutions will be fully resolving the baroclinic variations in the Southern Ocean and therefore will provide the most accurate simulations. While both these high-resolution versions were tested, in this thesis, I will only run experiments with the  $0.5^\circ$  and  $0.25^\circ$  longitude resolutions due to temporal constraints. This too low resolution is one of the caveats of the findings in this thesis (see chapter 6) and some of the model biases (section 3.7) might result from it—an issue that will be addressed in future endeavors.

### 3.4.2 Vertical grid & resolution

I introduced and described the stretched, terrain-following vertical coordinate system in ROMS (Song and Haidvogel, 1994; Shechetkin and McWilliams, 2003, 2005, 2009b) already in section 3.1.1. Here, I will discuss the parameters and the vertical resolution used for the Southern Ocean setup. This version of the coordinate system (version 3 of UCLA-ETH vertical coordinates) has the option to specify a critical depth  $h_c$ , the surface stretching parameter  $\theta_s$ , the bottom stretching parameter  $\theta_b$ , and the number of layers  $N$ . The lower most layers follow the terrain more closely than the upper layers (Figure 3.2c). The depth at which this transition occurs can generally be controlled by  $h_c$ . The deeper this level is, the flatter are the grid lines towards the surface. If  $\theta_s$  increases the number of layers and therefore the resolution increases towards the surface. The same holds for the bottom layers when increasing  $\theta_b$ .

I found that the results produced by KPP as well as the model drift in the water masses are inherently sensitive to the choice of parameters. The standard parameters used in most ROMS simulations are shown in gray in Figures 3.2a and b. Lowering  $h_c$  to 1000 m helped to preserve water masses due to a reduction in spurious mixing. However, this leads to a substantial reduction in resolution at the surface (inset of Figure 3.2a). Fewer layers at the surface led to larger biases in surface mixing processes, because KPP had less layers to fit the stability functions (section 3.2.2). In extreme cases this led to a complete disappearance of the surface mixed layer. Using a more reasonable value for  $h_c$  of 450 m and at the same time increasing  $\theta_s$  to its maximum of 10, improved both the surface mixing and water masses (blue in Figure 3.2). This is owing to a higher resolution, reduced tilting, and more evenly spaced layers towards the surface. Using a maximum value of 4 for  $\theta_b$ , allowed the resolution of the bottom boundary layer over more shallow regions. Note that the apparent low resolution of the bottom layers in Figure 3.2b is owing to the fact that

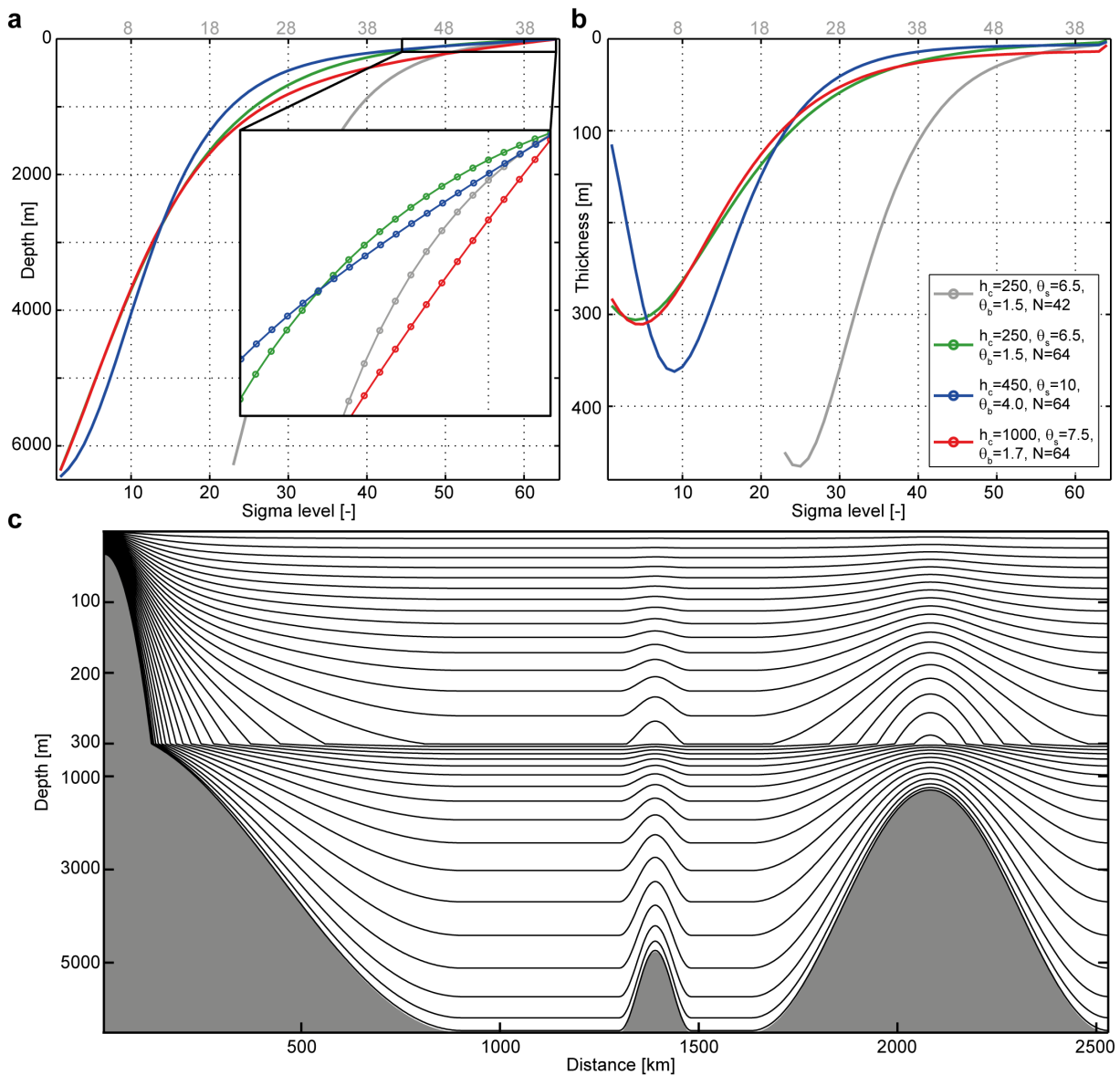


**Figure 3.2 Vertical grid in the Southern Ocean ROMS:** (a) Depth of vertical layers for different parameters of the vertical coordinate system at an ocean depth of 6500 m. The zoomed inset shows the top 200 m. (b) Vertical resolution of vertical layers for different parameters of the vertical coordinate system at an ocean depth of 6500 m. The final parameters used for the Southern Ocean model are shown in blue in a and b. (c) A vertical cross-section showing the final sets of parameters over an exemplary bathymetry (only every second layer is shown).

this figure is produced using the maximum ocean depth of 6500 m. In a more shallow region of about 500 m the bottom layers would have a vertical extent of about 8 m.

The performance of KPP improved considerably, especially in the deep ocean, when using more vertical layers (64 instead of 42). I chose 64 layers so that at least two layers were located in the upper most 10 m at the deepest location (6500 m). Such an increase of vertical resolution would theoretically lead to much higher computational expenses, not only due to the higher number of grid cells but also due to a much smaller time step, as the vertical motion became the limiting factor for not violating the *Courant-Friedrichs-Lewy* (CFL) criterion. This effect could be alleviated by using a new development that temporarily adjusts the time step on-line in the

model if the CLF criterion breaks in the vertical (Shchepetkin, 2015). In fact, the time step could be chosen much larger than previously when using this development allowing for a 50% higher vertical resolution at the same computational expense.

### 3.4.3 Topography & land-sea-ice mask

The bathymetry in the model (see Figure 3.3) is based on RTopo-1, which is a compilation of different data sets of the Antarctic continental shelf regions and ice shelf topographies merged into the global GEBCO bathymetry data set (Timmermann et al., 2010). The use of RTopo-1 is essential for an accurate ocean circulation in this setup. Previous attempts using ETOPO led to very large biases in the model that were largely induced by strong deviations in the bathymetry of up to several hundred meters over the Antarctic continental shelf between ETOPO or GEBCO compared to RTopo-1. Very recently, this data set was further improved to RTopo-2 (Schaffer et al., 2016). This update should be used in future applications.

I prepared the bathymetry for ROMS in multiple steps. I had to divide the grid into two parts as the *ROMSTOOLS* are not able to create a circumpolar bathymetry for the grid file. These two parts were overlapping and also extended on either side of the domain to ensure a smooth transition when merging them again and at the periodic boundary. Each of these two parts was processed in the same way. First, I used the Fortran-routine *etopo* of the *ROMSTOOLS* to average the 1-minute resolution topography from RTopo-1 onto the coarser ROMS grid without any smoothing. From the resulting bathymetry, I created a land-sea-mask by setting all grid points with a depth shallower than 5 m to land and enforcing connectivity between all ocean points to obtain a single ocean basin. Second, I re-applied the *etopo*-routine on RTopo-1 to average the bathymetry onto the ROMS grid, but this time applied a smoothing radius of 5 (ratio between characteristic smoothing width and local grid size). A value larger than one implies that the bathymetry is smoothed over multiple grid points. I found that using a value of 5 rather than a smaller value that I used originally helps to reduce spurious isopycnal mixing (section 3.1.1), because the vertical coordinates have a smaller local tilt, which can be better resolved by the model. In a final step, I applied the Fortran-routine *lsmooth* (conditional log-smoothing) of the *ROMSTOOLS* with an r-factor of 0.15, which ensures that the local slope can be resolved by the model. Through this routine, I also constrained the depth to a minimum value of 50 m and a maximum value of 6500 m. Especially, the former value helps to enhance the models stability.

Large parts of the Antarctic land-ice covered region are below sea level are covered by floating ice shelves or the grounded ice sheet. ROMS, in the version used here, does not include an ice-shelf cavity model but is forced with lateral fluxes from the ice shelves (see section 3.5.3). Therefore, the descent of the the ocean's surface under the ice shelves cannot be simulated. I here impose a vertical wall to the model at the ice-shelf edge by modifying the land mask. For this purpose, I interpolated the location of the land, ice shelves, and grounded ice sheet from RTopo-1

onto the ROMS grid using the CDO (2015) nearest neighbor interpolation. Any point covered by either one of these points in the interpolated mask was defined as land or ice in the final land-sea-ice mask of the grid file. The final bathymetry and land-sea-ice mask of the model are displayed in Figure 3.3. ROMS does not account for the so-called wetting and drying effects, which are a spill-over of land points as the sea level changes. Therefore, land points are never involved in any computation by the model and provide an effective lateral wall to the model.

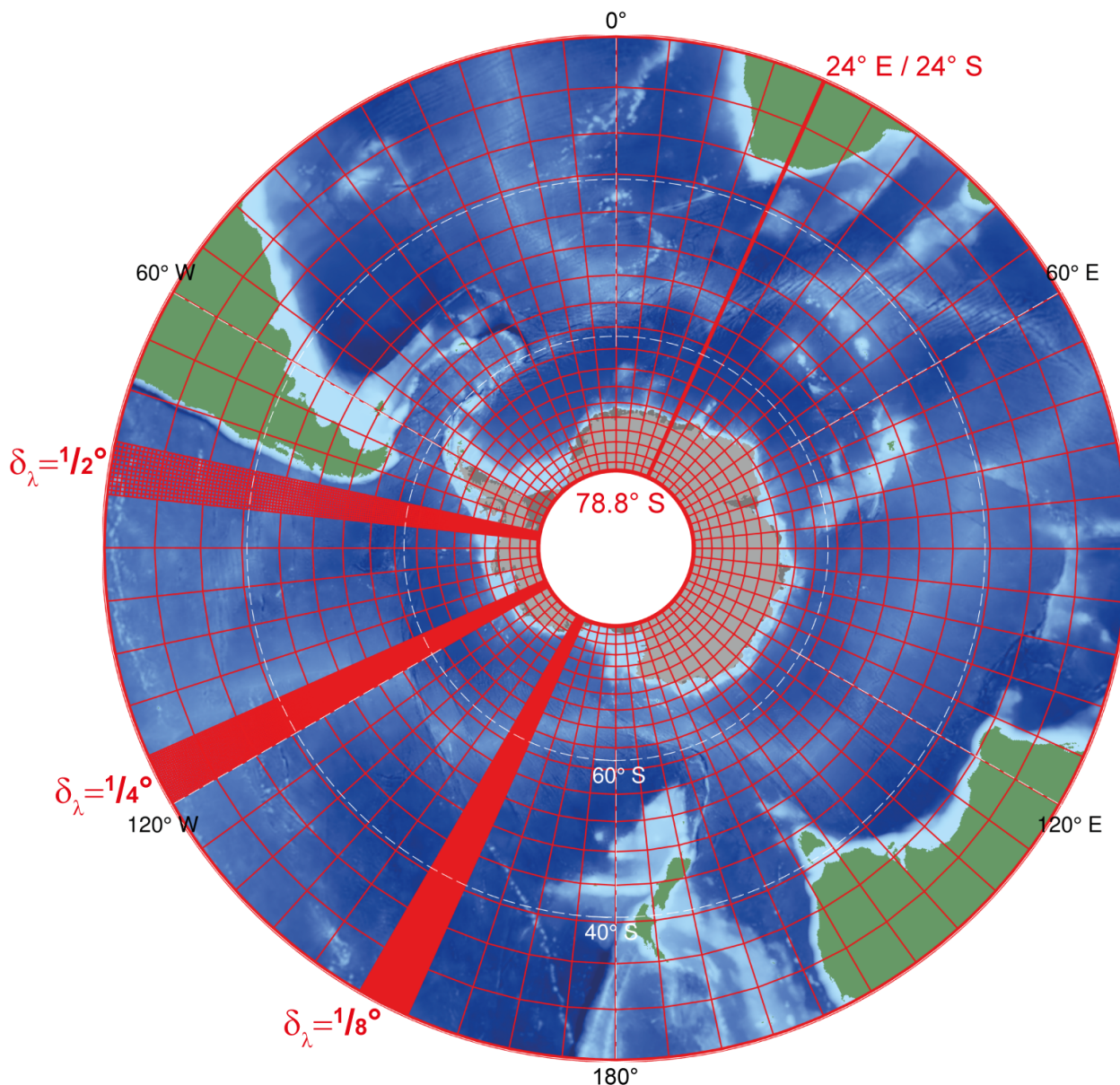


**Figure 3.3 Model grid, bathymetry, and land-sea-ice mask of the Southern Ocean ROMS setup:** The model grid is illustrated through the red lines that only show a few selected grid lines for illustration. The  $0.5^\circ$ ,  $0.25^\circ$ , and  $0.125^\circ$  zonal resolutions are shown as examples in small sectors. The thick red lines indicate the model domain boundaries to the north and south and the periodic boundary in the east-west direction. The background shows the ocean bathymetry and land-sea-ice mask in the model (see text for details). The lighter gray shows the grounded ice sheet and the darker gray the ice shelves.

## 3.5 Forcing

The model is forced at the surface with freshwater, heat, and momentum fluxes from either the atmosphere (section 3.5.1), sea ice (section 3.5.2), or land ice (section 3.5.3). The latter partly enters the model as a surface forcing, i.e., melting icebergs, and a subsurface forcing, i.e., melting ice shelves. The model is directly forced with fluxes rather than using a bulk formula. Some of these fluxes are modified while the model is running as I will describe in more detail below. Additional surface fluxes are induced by a surface restoring to the observed salinity and temperature fields (section 3.5.4), which is here used as a flux correction. At the open northern boundary the model is forced with observation-based momentum and tracer fields (section 3.5.5). All model forcings are monthly mean climatologies. To account for high-frequency variability, which are critical for e.g. mixing processes, daily anomalies from the year 2003 were superimposed on the climatologies of the surface fluxes to form a so-called normal year forcing, which has the same monthly means as the climatology but accounts for daily weather effects. Perturbations of this mean forcing that I used for the sensitivity studies will be described in the chapters 4 and 5.

### 3.5.1 Atmosphere–ocean fluxes

At the atmosphere–ocean interface, the freshwater, heat, and momentum fluxes are mostly from the ERA-Interim global atmospheric reanalysis produced by the European Center for Medium-Range Weather Forecasts (ECMWF) (Dee et al., 2011; ECMWF, 2007). Some modifications to these fluxes are described below. Air–sea fluxes in the Southern Ocean are associated with very large uncertainties mostly owing to the lack of observational data (Bourassa et al., 2013). In many respects, ERA-Interim provides to date probably the most reliable estimate of these fluxes (Bromwich et al., 2011; Nicolas and Bromwich, 2011; Trenberth et al., 2011; Bracegirdle and Marshall, 2012; Bracegirdle, 2013). Nevertheless, I will apply multiple corrections to mitigate some of the known biases and large uncertainties will remain in the air–sea fluxes.

I here use 6 hourly ERA-Interim data from the native reduced N128 Gaussian grid, which has a spectral resolution of T255. The variables are the surface net solar and net thermal radiation, the surface sensible and latent heat flux, the instantaneous eastward and northward turbulent surface stress, the evaporation and the total precipitation. The data is masked with the ERA-Interim land-sea mask to only include ocean points, using a threshold of 0.5 from the land-sea mask (ECMWF, 2007). I used *ROMSTOOLS* to interpolate the data onto the Southern Ocean grid. However, the original *ROMSTOOLS* performed this interpolation based on the longitude-latitude coordinate system. This procedure provides good results for lower latitudes, but returned large interpolation errors in higher latitudes due to the converges of the longitudes towards the pole. Therefore, I implemented a method that projects the data first onto a polar stereographic grid and then uses the effective spatial distance for the interpolation. The interpolation is then performed using a natural

neighbor method. Additionally, the missing land points were filled by a linear extrapolation from the ocean points. The latter ensures that each ocean point on the ROMS grid has an associated surface flux. Using this method, I first created monthly mean fields over the period 1979 to 2014, and then averaged them to a monthly climatology. Additionally, I created daily forcing data for the year 2003 and calculated the anomalies of these daily fields to the monthly mean fields of the same year. At last, I added the daily anomalies of the year 2003 to the monthly mean climatology of the years 1979 through 2014 to obtain a normal year forcing with weather effects from the year 2003 and mean fluxes of the entire climatological mean period.

Large uncertainties and potential biases exist in the atmospheric surface freshwater flux, which is the evaporation minus the precipitation fields (E-P, Figure 3.4a–c). While the mean distribution shows a reasonable pattern of an exceeding evaporation in the lower latitudes and exceeding precipitation in the higher latitudes, the strength of the net freshwater flux to the ocean in ERA-Interim is most likely overestimated in the polar frontal regions. This overestimation becomes apparent from a comparison to a satellite based estimate (HOAPS version 3.2; Andersson et al., 2010, see Figure 3.4b) and is also consistent with the findings by Cerovečki et al. (2011), who used a flux-correction method with the Southern Ocean State Estimate (SOSE). The integrated net atmospheric freshwater flux over the ocean south of 50° S amounts to about 0.65 Sv in ERA-Interim and about 0.35 Sv in HOAPS. The latter value is probably a slight underestimation, as the fluxes over sea ice are not included. The lower value from HOAPS is also consistent with the estimate by Abernathey et al. (2016), who calculated an amount of 0.28 Sv over the same region and an additional 0.14 Sv onto sea ice (total of 0.42 Sv) using the flux-corrected SOSE. I here correct for some of the apparent overestimation in ERA-Interim by using a correction factor of 80% and, additionally, by applying a salinity restoring flux (section 3.5.4) in the northern part of the domain. I also applied a spatial correction to the atmospheric surface freshwater flux over sea ice by redistributing the snow layer according to the observed sea-ice advection (section 3.5.2). The total amount of snow or precipitation falling onto the Antarctic sea ice in ERA-Interim is about 0.11 Sv, which is in line with the estimate by Abernathey et al. (2016) above. A key problem of reanalysis products in general is that the global moisture budget does not close (Trenberth et al., 2011; Lorenz and Kunstmann, 2012). However, ERA-Interim shows a reasonable global closure (Lorenz and Kunstmann, 2012), making it a more reliable product in terms of temporal changes of the surface freshwater fluxes (Bromwich et al., 2011; Nicolas and Bromwich, 2011). Trends in the ERA-Interim E-P over the Southern Ocean are very small over recent decades, which agrees with observation based products (see table 4 by Bromwich et al., 2011).

The surface heat flux forcing equals the sum all heat fluxes described above. Additionally, the net surface solar radiation flux is provided as a separate forcing field to ROMS as it penetrates into the surface ocean. This shortwave radiation is prescribed to the model on a daily basis. Hence, diurnal variations have to be parameterized in order to account for night-time cooling and day-time warming of the mixed layer. In previous versions of ROMS, the diurnal cycle was simply modified by a cosine function leading to problematic situations in high latitudes. Therefore, a

more accurate formulation was implemented to account for variations of the diurnal cycle with latitude. Additionally, a dependence on longitude was implemented for a correct timing of the diurnal cycle. ERA-Interim overestimates the net shortwave and underestimates the net longwave radiation (Dussin et al., 2016). I corrected the monthly mean fields for these biases using the difference between the original ERA-Interim and the DFS5.2 (Dussin et al., 2016) fields in areas without sea ice. Moreover, ERA-Interim has a warm bias of in the near-surface temperature in the coastal region of Antarctica of up to  $2^{\circ}\text{C}$  (Bracegirdle and Marshall, 2012; Mathiot et al., 2012), which would lead an insufficient heat loss from the surface ocean. In most regions this bias is irrelevant in my simulations as the surface heat flux in the sea-ice covered area is over-written by an under-ice heat flux computation (section 3.5.2). Nevertheless, this bias could lead to an underestimation of the heat loss in some coastal polynya regions.

The large-scale circulation is generally well represented in ERA-Interim (Bracegirdle and Marshall, 2012; Bracegirdle, 2013; Sanz Rodrigo et al., 2013). Biases might exist in coastal regions, where the effect of local topographic wind systems is underrepresented. Such a bias is a common problem in coarse resolution atmospheric models. However, it mostly affects the ocean through the formation or absence of polynyas and sea-ice production (Mathiot et al., 2010, 2012; Stössel et al., 2011). As the sea-ice forcing of the ocean is prescribed in my simulations (section 3.5.2), this latter bias does not have an influence on the simulations. However, it might have an influence on wind-driven transport and mixing processes on the continental shelf.

BEC is forced with the climatological mean atmospheric partial pressure of  $\text{CO}_2$  from the period 1998 to 2011 (Landschützer et al., 2014a). Additionally, surface deposition of iron and dust are used from the global model CCSM (Mahowald et al., 2009) and corrected for the deposition on sea ice (section 3.5.2).

### 3.5.2 Sea-ice–ocean fluxes

The UCLA-ETH version of ROMS—in contrast to the Rutgers version of ROMS and BRIOS mentioned earlier (see section 3.1)—is not coupled to a sea-ice model and I will not use one in this thesis. Nevertheless, as part of this project, I have partly implemented the sea-ice model by Budgell (2005) from the Rutgers version of ROMS (updated and maintained by K. Hedström). This sea-ice model has both a thermodynamic and dynamic component. The thermodynamics follow the formulation by Mellor and Kantha (1989) and Häkkinen and Mellor (1992). The model consists of two sea-ice layers, one snow layer, and one molecular sublayer beneath the sea ice. Frazil ice formation according to Steele et al. (1989) occurs when the ocean surface reaches the freezing point temperature. The sea-ice dynamics use the elastic-viscous-plastic (EVP) rheology by Hunke and Dukowicz (1997) and Hunke (2001). As the use of a thermodynamic-dynamic sea-ice model became obsolete throughout this thesis, I postponed the finalization of the implementation to future developments.

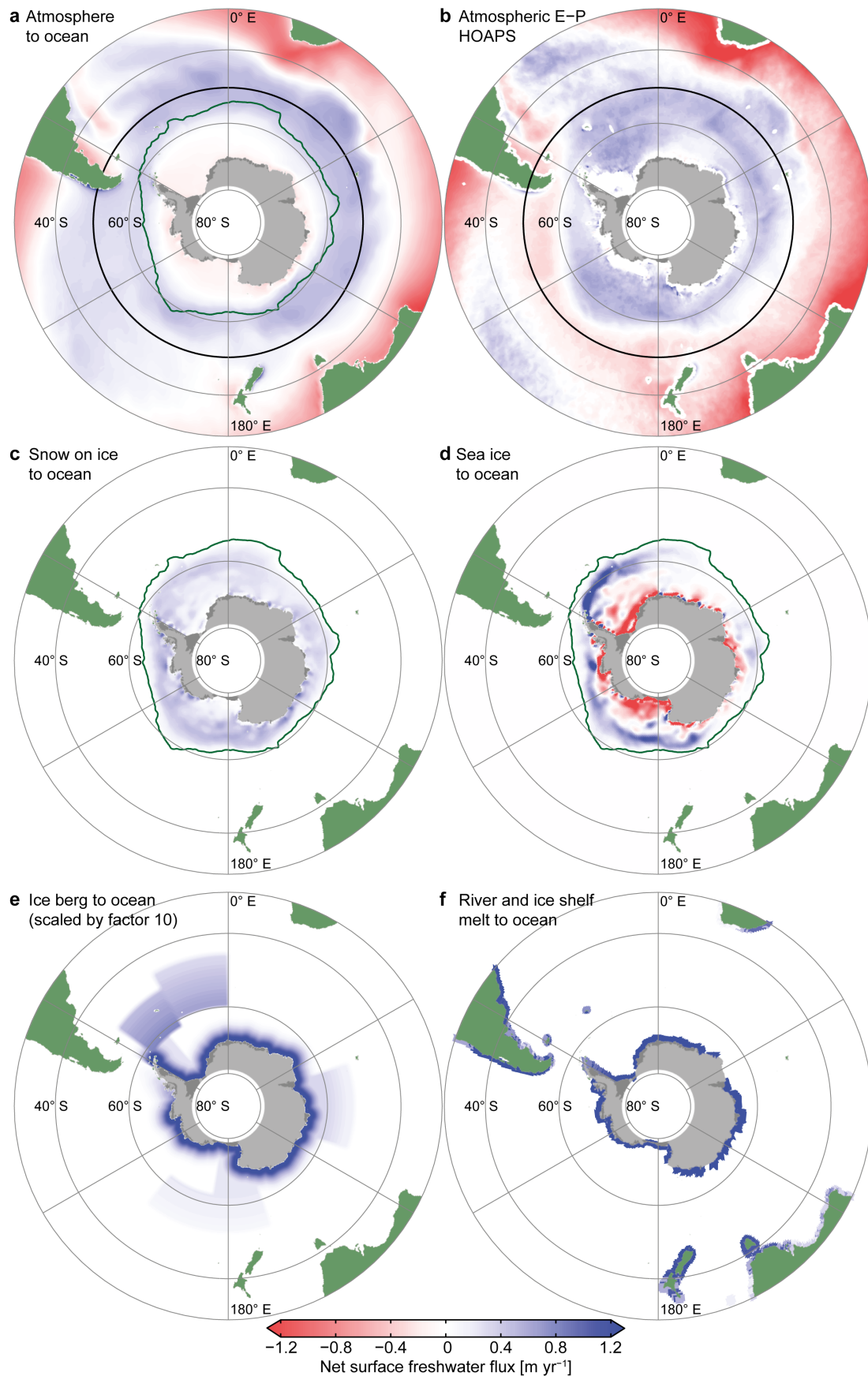


**Figure 3.4 Surface freshwater flux forcing components:** (a) Net annual atmosphere–ocean flux (E–P) modified from ERA-Interim. (b) Net annual atmospheric freshwater flux (E–P) HOAPS (compare to a+c). (c) Annual snow melting flux from sea ice. (d) Net annual freshwater flux from sea-ice formation and melting. (e) Net annual freshwater flux from iceberg melting (scaled by a factor 10). (f) Net annual land ice melting and river runoff (grid points are magnified). Green contour: climatological mean sea-ice edge; black line: 50° S. See text for details.

At the sea-ice–ocean interface, my approach differs from previous forced, regional modeling studies of the Southern Ocean. Instead of using a thermodynamic-dynamic sea-ice model, in this thesis, I will make use of the observation based ice–ocean surface fluxes derived in chapter 2. The main reason is that accurate simulations of sea ice in the Southern Ocean are very difficult and biases in the sea-ice fluxes can substantially influence the water-mass structure in the Southern Ocean. The difficulty of obtaining accurate sea-ice simulation is mostly owing to highly dynamic nature of the sea ice in this region (Emery et al., 1997; Haumann, 2011) and the Southern Ocean sea-ice dynamics are not well represented in models (Haumann et al., 2014; Uotila et al., 2014; Lecomte et al., 2016). This can lead to biases in the lateral transport of freshwater by sea ice, affecting both AABW and AAIW formation (see chapter 2). Moreover, there are strong atmosphere-ice-ocean feedbacks (Curry et al., 1995; Zhang, 2007; Liu and Curry, 2010; Stammerjohn et al., 2012) that can lead to large deviations in the sea-ice cover if there are only small inaccuracies in the atmosphere or ocean. As a consequence of these difficulties, coupled models notoriously suffer from very large biases in the sea-ice cover of the Southern Ocean (Mahlstein et al., 2013; Turner et al., 2013; Zunz et al., 2013). One particular issue that often leads to a very different water-mass structure in coupled models is the occurrence of spurious open-ocean polynyas and deep open-ocean convection (Stössel et al., 2015). Another common problem is the representation of coastal winds and the associated coastal polynya formation, which can alter the shelf water properties and therefore the AABW formation and ocean circulation (Petrelli et al., 2008; Mathiot et al., 2010; Stössel et al., 2011; Mathiot et al., 2012; Zhang et al., 2015).

In this study, I will prescribe the sea-ice concentration and the sea-ice–ocean freshwater fluxes (CPP-switch *ICEOBS*), because constraining the ocean circulation model with such a sea-ice forcing circumvents the problems described in the previous paragraph. Previous studies by Markus (1999) and Dinniman et al. (2003, 2007) have shown that prescribing the sea-ice cover can be great advantage when modeling the Southern Ocean surface and coastal waters. However, these studies calculated the sea-ice–ocean freshwater fluxes from the conductive and open-ocean heat fluxes and did not directly account for lateral advection of the sea ice, which redistributes the freshwater in the Southern Ocean (Haumann et al., 2016b). Therefore, additionally to the sea-ice cover, I here prescribe the climatological (1982–2008) daily mean sea-ice–ocean freshwater fluxes derived in chapter 2 (Figure 3.4d). The freezing fluxes were scaled so that the total annual freezing rate matches exactly the total annual melting rate in order not to induce any artificial model drift. The freezing and melting fluxes were both reduced by 10% to account for snow-ice formation (section 2.2.3), which would be part of the atmospheric forcing, even though the uncertainties in these fluxes are far larger than any of these effects (section 3.5.1).

The presence of a snow layer is calculated from the surface forcing prior to the model simulations (Figure 3.4c). For this purpose,  $E - P$  is split in all grid boxes with ice into  $E$  and  $P$ . ERA-Interim evaporation already accounts for the sea ice fraction (ECMWF, 2007). Hence, there is no need to modify it. I scaled  $P$  with the ice concentration, which means that  $P \cdot (1 - c_i)$  goes into the ocean and  $P \cdot c_i$  is accumulated in an artificial snow layer over the year. The resulting

annual snow layer is then scaled with the ice export fraction obtained by Haumann et al. (2016b) to redistribute it. The freshwater is then added to the forcing as the snow melts. This melting is computed in a first step using the atmospheric surface heat flux, which is used when it is positive to melt the snow layer. The residual snow layer is then in a second step melted by scaling it with the sea-ice melt, assuming that the heat is provided from the ocean. The same procedure is applied to the surface iron and dust deposition on sea ice.

All surface freshwater fluxes are added to the surface layer of the model and converted to a salt flux depending on the surface ocean salinity. The melting and freezing fluxes from sea ice are treated separately from the other fluxes in order to allow for subsequent parameterizations such as the convection of brine plumes (section 3.2.2) or to optionally use the sea ice production for the computation of heat fluxes (see below). All freshwater fluxes, including the sea-ice freshwater fluxes, enter the dilution of other tracers in the model at the surface.

The sea-ice concentration forcing field is the satellite observed sea-ice concentration ( $c_i$ ). Here, I will use the same CDR Bootstrap record that I also used to derive the freshwater fluxes (section 2.2.2). I replaced the sea-ice concentration field in the forcing files that was created from ERA-Interim data by the *ROMSTOOLS* with this data set, as the ERA-Interim provided sea-ice concentration suffers from multiple problems (Haumann, 2011) and to be consistent with the freshwater forcing.

The surface momentum forcing is modified under the sea ice to account for the atmosphere–ice–ocean momentum transfer. Due to the absence of lateral boundaries and the thin nature of Antarctic sea ice, it is in most regions at free drift. At free drift the momentum equation for sea ice can be simplified to (Omstedt et al., 1996; McPhee, 2008; Leppäranta, 2011):

$$\vec{u}_i = \vec{u}_w + N_a \vec{u}_a . \quad (3.8)$$

Here,  $\vec{u}$  is the velocity vector for ice, water, and air respectively and  $N_a$  is the so-called Nansen number that is defined through the ratio between the atmospheric and oceanic drag. The latter number is generally small and about 3% for Antarctic sea ice. Given the uncertainty and potential underestimation of the surface momentum forcing (section 3.5.1) and as I am here only interested in the oceanic momentum, I will safely neglect the reduction of the momentum stress by sea ice if the sea-ice concentration is below 90%. However, as soon as the sea-ice gets more compact, i.e. if there is a high ice concentration, internal sea-ice stresses start to play a role in the momentum balance and the amount of momentum that is transferred from the atmosphere to the ocean decreases, which can also be interpreted as an increase of the Nansen number (Lu et al., 2016). I here use a simplified representation of this effect by linearly decreasing the stress for high sea-ice concentrations. Therefore, I apply a factor of 1 to the momentum stress for an ice concentration of 90% or smaller and decrease this factor to 0.1 for an ice concentration of 100%. This drastically simplified approach might be further improved in future simulations.

The surface heat flux is modified in two steps, whereas the first step is performed on the forcing field and the second step throughout the model simulation. I will build this modification on the premise that the sea ice forms from the atmospheric cooling (heat flux) and melts from the ocean heat flux, which is a good assumption for most of the Antarctic sea ice (Gordon and Huber, 1990; Gordon, 1991; Martinson, 1990, 1991). Therefore, in the first step, the total amount of latent heat of freezing  $H_{if}$  is subtracted from the surface heat flux and is defined through:

$$H_{if} = \rho_i L_i P_{if} , \quad (3.9)$$

where  $\rho_i$  is the density of sea ice ( $925 \text{ kg m}^{-3}$ ),  $L_i$  is the specific latent heat of melting and freezing ice ( $334 \cdot 10^3 \text{ J kg}^{-1}$ ), and  $P_{if}$  is the sea-ice formation rate. The result is then multiplied by the inverse sea-ice concentration. I also subtract the amount of shortwave radiation that is absorbed by sea ice and only add the fraction that is absorbed by the ocean back to the net surface heat flux. For the latter calculation I used constant values for the sea-ice and ocean albedo of 0.85 and 0.06 respectively to be consistent with the original ERA-Interim formulation (ECMWF, 2007). At last, I subtract the latent heat flux that is used for melting snow and icebergs. The resulting product contains the sole net atmosphere–ocean heat flux in open water. The surface air temperature in ERA-Interim has a pronounced warm bias (see section 3.5.1), which most likely leads to an underestimation of the surface cooling in open water areas in high-latitudes. This bias might be corrected for in future simulations by using a bulk formula and correcting the surface temperature.

The second step of the heat flux modification is performed online during the simulation to account for the ice–ocean flux ( $H_i$ ) in the ice covered ocean. For this calculation, I follow the approach by Markus (1999):

$$H_i = \rho_0 c_p c_h u^* (T_f - T_N) \quad (3.10)$$

$$= \frac{k_i k_s (T_a - T_f)}{k_i h_s + k_s h_i} + \rho_i L_i P_i . \quad (3.11)$$

In equation 3.10,  $\rho_0$  is the reference density of the model ( $1027 \text{ kg m}^{-3}$ ),  $c_p$  the specific heat capacity of seawater ( $3985 \text{ J kg}^{-1} \text{ K}^{-1}$ ),  $c_h$  is the heat transfer coefficient with a value of 0.0055 (Stanton number McPhee, 1992),  $u^*$  the friction velocity,  $T_N$  the temperature of the upper most model layer, and  $T_f$  the freezing point temperature, defined through (Steele et al., 1989):

$$T_f = -0.0543 S_N , \quad (3.12)$$

where  $S_N$  is the salinity of the model's surface layer. In equation 3.11, the first term denotes the conductive heat flux through the ice and the second term the latent heat of sea-ice formation and melting (see equation 3.9). Here,  $k_i$  ( $2.04 \text{ W m}^{-1} \text{ K}^{-1}$ ) and  $k_s$  ( $0.31 \text{ W m}^{-1} \text{ K}^{-1}$ ) are the heat conductivities of sea ice and snow, and  $T_a$  is the atmospheric surface temperature (Markus, 1999).

Markus (1999) calculates  $H_i$  according to equation 3.10 and uses equation 3.11 to calculate the sea-ice production and the associated freshwater flux. In this case, the ice–ocean freshwater fluxes depend on the ocean vertical heat exchange. However, here I am interested in the response of the ocean to the observation based surface freshwater fluxes that are used to force the model. Consequently, I could constrain  $H_i$  either through equation 3.10 or 3.11, both having their advantages and disadvantages. The use of 3.11 is influenced by biases in the atmospheric temperature, ice and snow thickness, and uncertainties in the ice production. In a first attempt, I used such a formulation of the surface heat flux. However, this led to large warm biases in the high-latitude surface ocean, mainly due to the warm bias in ERA-Interim data. Therefore, I here decided to use 3.10. The use of equation 3.10 is associated with different challenges. These are the influence of biases in the vertical mixing of heat and uncertainties in  $u^*$ . A more ideal implementation in future would be to accurately compute the  $H_i$  from equation 3.11 using a bias corrected surface air temperature and reasonable estimates for the sea-ice and snow thickness. This flux could be computed offline since the sea-ice melting and freezing fluxes observation based.

In the model the surface heat flux is additionally constrained, so that the model’s surface temperature does not drop below the freezing point, which is computed through equation 3.12.

### 3.5.3 Land-ice–ocean fluxes

As for the sea ice, there is no explicit land ice component in ROMS that would simulate the interaction between the ocean and the ice shelves of the Antarctic continent. Yet, the melting of land ice is an important contributor to the water-mass transformation on the continental shelf that also contributes to the formation of AABW (Gordon, 1991, 2012, 2014; Jacobs, 2004). Land ice melting changes the water properties through a removal of sensible and latent heat from the ocean (buoyancy loss) and a net addition of freshwater to the ocean (buoyancy gain).

Spatial variation of these sources and sinks determine different varieties of shelf waters and AABW found around the Antarctic continent. Therefore, ideally, in a model, the sources should vary as well. Another important factor is the partitioning of the melting between basal melting at the ice shelf edge and melting of icebergs that can drift and spread the melt water over a large distance (Silva et al., 2006; Tournadre et al., 2016). The partitioning between these two sources is about equal in a circumpolar sum but varies regionally (Depoorter et al., 2013; Rignot et al., 2013). In order to represent these fluxes as realistically as possible, I here force the model with spatially varying, observation-based estimates of iceberg and ice shelf melting rates for each ice shelf of the Antarctic continent (Depoorter et al., 2013).

I add iceberg fluxes directly to the surface forcing of freshwater and heat (Figure 3.4e; note that the iceberg flux is scaled by a factor of 10 in the figure). At this point in time the iceberg melting is not yet affecting the biogeochemistry through the input of nutrients and other tracers,

which should be implemented in future developments. The melting is distributed over the Southern Ocean following approximately the satellite-observed trajectories by Silva et al. (2006) and decreasing with distance from the coast, so that about 60% melt south of 63° S (see Figure 3.4). I scaled this spatial melting pattern in time using the shortwave radiative flux. A more sophisticated method would be to couple the model to an ice-berg trajectory model as suggested by numerous studies (Gladstone et al., 2001; Martin and Adcroft, 2010; Marsh et al., 2015; Merino et al., 2016). As such data sets are now available and are probably more realistic than my reconstruction, they should be used in future improvements of the surface forcing for this model. Ultimately, the magnitude of the total ice-berg melting fluxes is with about 0.04 Sv (Depoorter et al., 2013) very small compared to the other surface fluxes (sections 3.5.1 and 3.5.2). Therefore, their exact spatial pattern is not that essential in my simulations. However, it is important to move the iceberg melt away from the coastal grid cells. If all the melting was imposed in the coastal region, this would lead to a reduction in bottom water formation on the shelf (Martin and Adcroft, 2010; Stössel et al., 2015) and might enhance spurious open-ocean convection (Stössel et al., 2015; Merino et al., 2016).

A wide range of ways to represent basal ice-shelf melting exists in models. In coupled global models, these processes are vastly underrepresented and it is common practice to simply add the precipitation over Antarctica as runoff to the surface waters along the coast or spread it over a certain area (Marsland and Wolff, 2001; Stössel et al., 2015). A better, yet very simple, parameterization for coarse resolution was suggested by Beckmann and Goosse (2003), which calculates fluxes along the ice-shelf edge without the need to resolve the actual ice-shelf cavity. In higher-resolution models, ice-shelf cavity models (Holland and Jenkins, 1999) have been implemented and produce realistic melting rates around Antarctica (Timmermann et al., 2012; Hellmer et al., 2012; Goldberg et al., 2012; Timmermann and Hellmer, 2013; Nakayama et al., 2014). Such an ice-shelf cavity model was implemented into the Rutgers version of ROMS (Dinniman et al., 2007, 2012) and might be adapted for this version of ROMS in future.

In order to make use of the observation-based estimates of basal melting rates (Depoorter et al., 2013), I here implement a new option to ROMS (CPP-switch *TSOURCE*) that allows the addition of sources of water and associated tracer fluxes in the model interior anywhere in space and time. This new option reads the forcing data of freshwater volume, heat and tracer fluxes as four dimensional fields from a separate forcing file. In the model, the freshwater volume that is added dilutes all tracers and adds the additional tracer fluxes if they are provided as if they were advected into the grid cell. The implementation of these sources allows the addition of the freshwater and heat from ice-shelf melting to be spread over a certain depth range in the subsurface ocean and for each ice shelf separately. I created the forcing files by first spreading the estimated melt water of each ice shelf (Depoorter et al., 2013) in the horizontal direction along the first ocean grid cell off the ice-shelf edge that is given by the ice-shelf mask from RTopo-1 (see section 3.4.3). As these fluxes are representative of the year 2009, I lowered the meltwater input in the Amundsen and Bellingshausen Seas according to the suggested trends in the 1990s

and 2000s by Sutterley et al. (2014) and Paolo et al. (2015), which amounts to an integrated flux that is about 40% lower. So far, to my knowledge, there is no evidence for a significant trend in these fluxes prior to 1992, which I will use here as a climatological mean state (Figure 3.4f). In a second step, I scaled the total flux of each grid cell with the size of the grid boxes in the vertical and equally distributed the flux from 50 m depth to the bottom of the ocean to mimic the ice-shelf cavity. Adding the fluxes to the surface would lead to a too strong salinity stratification and inhibit the melt water from being mixed down, leading to too salty bottom waters. In the same way, I added the corresponding latent and sensible heat fluxes. For the sensible heat flux, I assumed that the ice that is melted had to be warmed from  $-20^{\circ}\text{C}$  to the melting point temperature. As the seasonal cycle of these fluxes is unknown, I used a constant annual mean flux throughout the year. The way that I implemented the basal melting does not allow the study of feedbacks between changes in the ocean and changes in the melting rate. However, it allows the study of the ocean response to an increases in basal ice-shelf melting observed over recent decades (Sutterley et al., 2014; Paolo et al., 2015).

Similar to the ice-shelf flux, I spread the estimated climatological annual river runoff from the GRDC (2014) data base to the first ocean grid box along the coast line (Figure 3.4f). However, in contrast to the ice-shelf flux, I added the river runoff to the surface forcing rather than distributing it vertically over the water column.

### 3.5.4 Restoring

During the simulations, I used a restoring of the surface salinity and temperature fields. This procedure helps to reduce biases in the surface forcing (Figure 3.4) and keeps the model from drifting strongly (section 3.6). Note that during the perturbation experiments the surface restoring is treated separately in order not to affect the model's response, which is discussed in chapters 4 and 5.

Surface salinity is restored to the monthly mean satellite observed surface salinity from Aquarius (version 4) over the period 2011 through 2015 (NASA Aquarius Project, 2015). As the salinity in higher latitudes is not available or not reliable, I only use a restoring north of  $48^{\circ}\text{S}$  and linearly decrease it towards  $53^{\circ}\text{S}$  (Figure 3.5c). The restoring time scale for the surface salinity is set to  $0.022\text{ d}^{-1}$ . In future efforts, a restoring towards the surface salinity from e.g. ARGO data might further improve the high-latitude surface freshwater fluxes. Yet, such products exist mostly on an annual rather than monthly basis (CARS ARGO only; Ridgway et al., 2002). Potential products that might be tested are either the MIMOC climatology (Schmidtko et al., 2013) or the climatological monthly mean salinity (Zweng et al., 2013) fields from the 0.25° version of World Ocean Atlas 2013 (WOA13 Boyer et al., 2013).

The surface heat flux in ROMS is adjusted by restoring the surface temperature in the model to

an observed sea-surface temperature (SST) through a restoring term that varies in space and time and is referred to as the kinematic surface net heat flux sensitivity to the SST. This restoring term is calculated in the *ROMSTOOLS* from the SST and the atmospheric surface temperature, density, wind speed, and specific humidity. Originally, this routine used monthly mean COADS data. However, the resulting restoring field in ROMS was of very poor quality in the high latitudes of the Southern Ocean. Therefore, I updated this routine to use the monthly mean NOAA Optimum Interpolation SST from AVHRR (Reynolds et al., 2007) over the period 1982 to 2014 and monthly mean ERA-Interim data for the atmospheric variables (Dee et al., 2011; ECMWF, 2007) over the same time period. No SST restoring is applied in areas covered by sea ice as data is less reliable.

### 3.5.5 Lateral boundary conditions

At the open northern boundary the model is forced with the climatological monthly mean temperature (Locarnini et al., 2013) and salinity (Zweng et al., 2013) fields from the 0.25° version of World Ocean Atlas 2013 (WOA13 Boyer et al., 2013) and ocean currents and sea-surface height data from the Simple Ocean Data Assimilation (SODA; version 1.4.2; Carton and Giese, 2008). The latter might be updated to SODA version 3 in future, which has the advantage of being consistent with the ERA-Interim surface forcing. BEC is forced with nutrient (Garcia et al., 2014b) and oxygen (Garcia et al., 2014a) fields from WOA13; dissolved inorganic carbon and alkalinity from the Global Data Analysis Project (Key et al., 2004; Lee et al., 2006); iron, ammonium, and dissolved nutrients from a global model simulation with CESM1.2 (Yang et al., 2017); and chlorophyll-a from the SeaWiFS climatology (SeaWiFS Project, 2003), which is extrapolated to depth according to Morel and Berthon (1989) and used for all phytoplankton functional types. I interpolated these fields onto the ROMS grid using a bi-cubic interpolation method from CDO (2015, version 1.6.8). ROMS has the possibility to either nudge the solution towards a given field over several grid boxes at the boundary or to use a prescribed boundary condition at the edge of the domain. Here, I use the latter and all tracers and the velocity are prescribed only at the northern most grid cells in the model. Therefore, the interior of the domain consists of a completely free running model.

I here use a radiation boundary condition for all tracers and the baroclinic mode that follows Orlanski (1976) and Raymond and Kuo (1984) and was implemented into ROMS by Marchesiello et al. (2001). This boundary condition radiates waves generated in the model domain out of the domain. It generally works well when the motion or wave propagation is exerted perpendicular to the boundary, which is the reason why the location of the northern boundary in the center of the subtropical gyres is of advantage (section 3.4). The barotropic mode and sea-surface height are imposed using the radiation boundary condition based on Flather (1976). However, the application of such a radiation boundary condition for the barotropic mode turned out to cause large model biases and model drift. These problems were visible in a drifting sea-surface height and

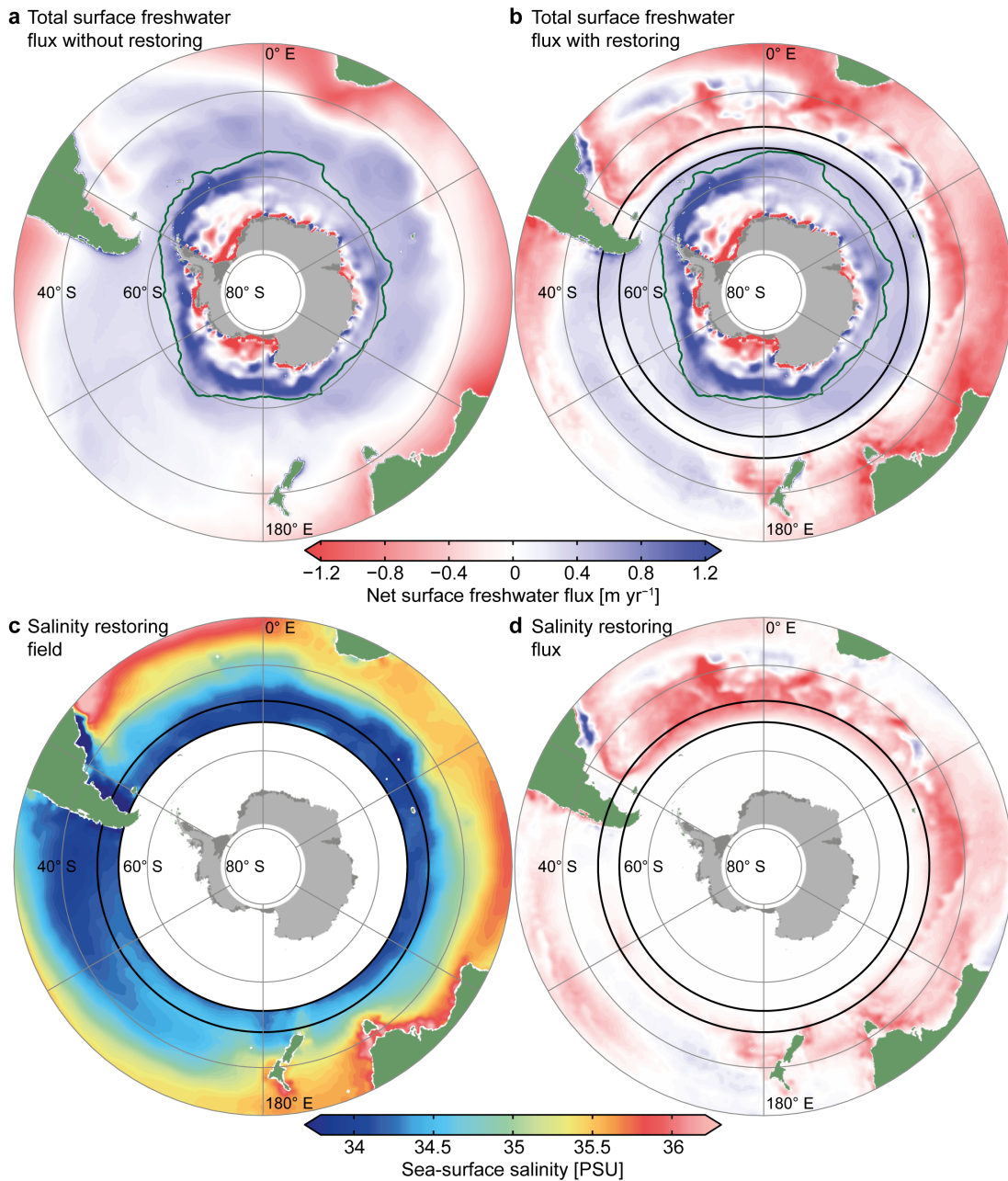


**Figure 3.5 Total surface freshwater flux forcing with and without restoring:** (a) Net annual total surface freshwater forcing without restoring flux. (b) Net annual total surface freshwater forcing with restoring flux. (c) Modified Aquarius sea-surface salinity field used for freshwater flux restoring. (d) Net annual surface restoring flux from the simulation years 21 to 40. Green contour: climatological mean sea-ice edge; black lines: 48° S and 53° S. See text for details.

a continuous northward displacement of the ACC. The key problem that I identified was that the model was open to all three ocean basins in the north, but had no knowledge on the mass exchange between these basins north of the model boundary. Therefore, it was free to change the mass balance between the ocean basins without knowing that the net exchange at the northern boundaries had to equal the trough-flow in the Bering Strait (1 Sv; Ganachaud and Wunsch, 2000) in the Atlantic, and the Indonesian Throughflow in the Indian Ocean (11 Sv; Stammer et al., 2003; Naveira Garabato et al., 2014). In order to solve this problem, I only apply the radiation condition in the Atlantic and specify the barotropic transport at the northern boundaries in the Pacific and Indian

Ocean to the fixed value provided by the boundary condition. While this solution works well, it has the disadvantage of trapping barotropic waves in the model domain. Such effects would mostly occur in the more narrow Atlantic basin, which is the reason for applying the radiation boundary condition in this basin. Additionally, I dampened trapped barotropic waves by applying a sponge layer with a viscosity of  $400 \text{ m}^2 \text{ s}^{-1}$  over the northern most  $10^\circ$  of latitude (10 and 20 grid cells in the  $0.5^\circ$  and  $0.25^\circ$  configurations, respectively). In sum, these modifications allowed for an accurate simulation of the ocean circulation in the interior of the domain. In practice, the ROMS setup that I use here has compared to other regional domains a very good boundary with very little boundary artifacts such as strong along-boundary currents.

At the continental boundaries within the domain, ROMS imposes a free slip condition. While there is a setting in ROMS to use a no-slip condition, this condition only applies to closed domain boundaries but not the boundaries along the land-sea mask. However, implementing a partial slip condition along the continents might be useful in future to reduce e.g. overestimated coastal currents. The latter effect can be partially mitigated by using a bottom boundary layer and tuning the roughness length—a method that I applied here (section 3.2.2).

### 3.6 Computation, initialization, spin-up & model drift

The model runs with a calendar of 360 days and all months have an equal length of 30 days. Averages are written to the output for each month throughout the simulation. For the  $0.5^\circ$  model version, I found an ideal stable time step of 2700 s and for the  $0.25^\circ$  model a time step of 1200 s. I performed all simulations in parallel computing mode using the Message Passing Interface library Open MPI (version 1.6.5) on the ETH cluster *EULER* at the Swiss National Supercomputing Center (CSCS). The model's FORTRAN-77 code is compiled on *EULER* using the Intel<sup>®</sup> Ifort<sup>™</sup> compiler (version 14.0.1). *EULER* uses the Linux CentOS 6.5 operating system and computes on multiple Hewlett-Packard BL460c Gen8 nodes with two 12-core Intel<sup>®</sup> Xeon<sup>®</sup> E5-2697v2 processors (Extended Memory 64 Technology) each. The model reads and writes data from and to Network Common Data Form files (NetCDF-4, version 4.3.1; using HDF5 library, version 1.8.12). Input and output fields are partitioned into horizontal tiles and each core computes one tile. The model performs most efficiently if the number of grid cells per tile in the  $\xi$ -direction is about 10 times larger than the number of grid cells per tile in the  $\eta$ -direction. Test experiments showed that an optimal performance is achieved for about 100 grid cells per tile in  $\xi$ -direction, which approximately corresponds to the recommended tiling provided in Table 3.1. However, the model scales reasonably well for multiples of the suggested tiling if a faster computation is required. Using the suggested settings the physical  $0.5^\circ$  model can be integrated at a speed of 5 model years per hour. If the model is coupled to BEC the computation time increases by a factor of 3. However, it should be noted that these computation times strongly depend on the number of variables and the averaging period of the data written to the output files. Therefore, a large number of variables, e.g. written by BEC, can considerably slow down the simulation.

ROMS is initialized from rest, i.e., all velocities at the beginning of the simulations are set to 0. Similarly, the sea-surface height is also initialized at 0. All tracers are initialized with the climatological mean fields described in section 3.5.5. The temperature and salinity tracers are initialized with the January climatological mean fields. Starting the model with austral summer-time conditions has the advantage that more observational data enter the initial fields.

Throughout this project, I ran more than 200 simulations (mostly 10 years) with the low-resolution ( $0.5^\circ$ ) version of the physical model to test certain parameterizations, forcings, and model developments. Very often biases in the model only occur after several years of integration. However, these test simulations were feasible as the model is running very fast and computationally efficient, i.e., 10 model years in two hours on 288 cores.

For this thesis, I performed a 40-year spin-up simulation with both the physical  $0.25^\circ$  version and the coupled physical-biogeochemical  $0.5^\circ$  version of the model as a starting point for the experiments presented in chapters 4 and 5, respectively. Due to biases in the forcing data and inaccuracies in the model's representation of physical processes through parameterizations, the model drifts away from the observation-based initial conditions in the first years of the simulation

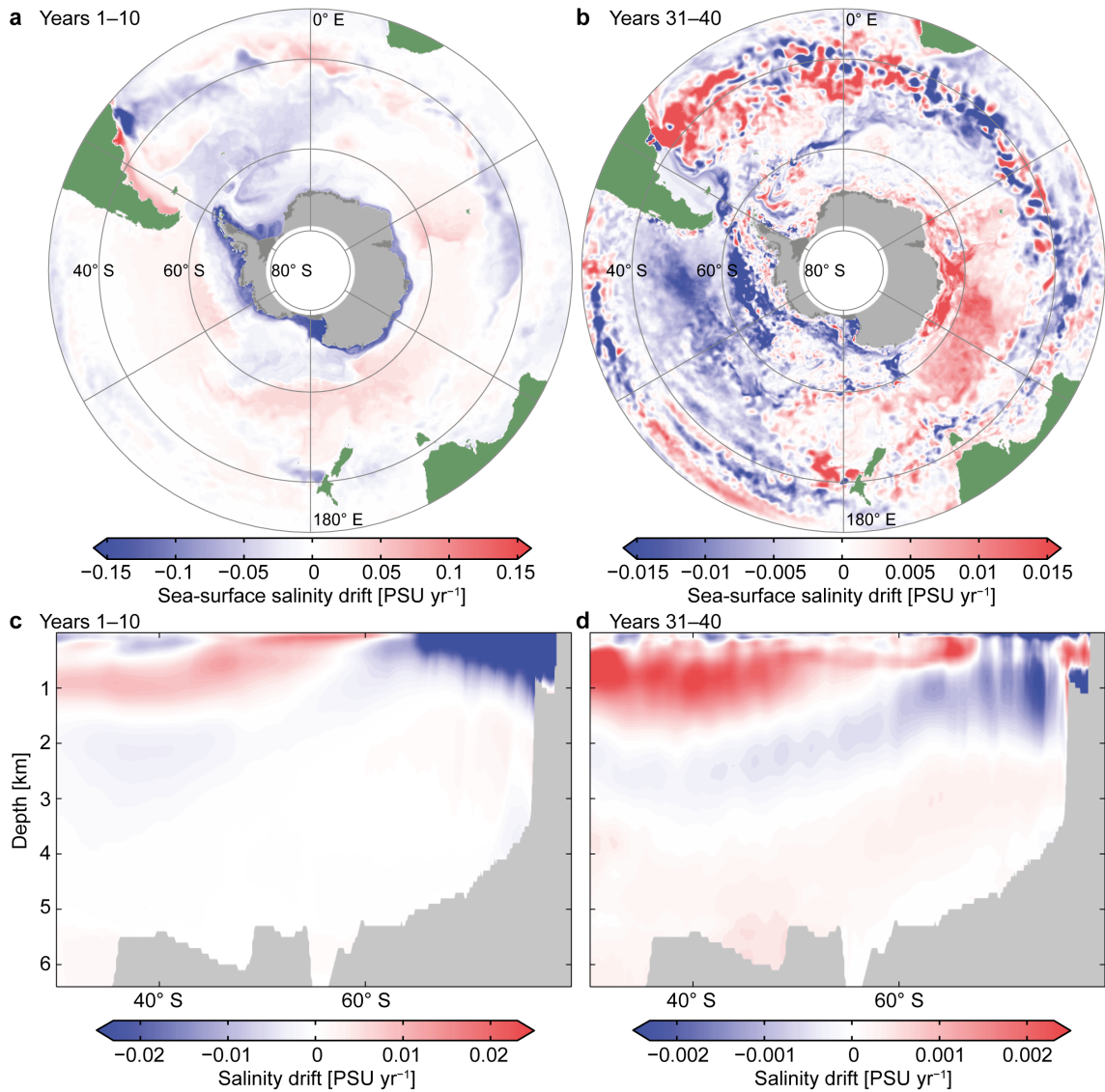


**Figure 3.6 Salinity drift during spin-up simulation:** Sea-surface salinity during simulation years 1 to 10 (a) and 31 to 40 (b). Cross-sections showing the zonal mean subsurface salinity drift during simulation years 1 to 10 (c) and 31 to 40 (d). Note the different scales.

towards a new equilibrium that is consistent with the forcing and model code (Figures 3.6, 3.7, and 3.8). Typically, a larger drift occurs in the first 10 years of the simulation and is about one order of magnitude smaller after the 40 spin-up years (note the different scales in Figures 3.6 and 3.7).

Strong drift occurs in the salinity fields over the continental shelf around Antarctica at the beginning of the simulation (Figure 3.6a,c). There are three potential reasons for this drift. Firstly, the WOA13 field that is used to initialize the model is a climatological mean over many decades, but the land ice melting (section 3.5.3) is estimated for the year 1992, which is a potentially higher melt rate than what would be consistent with WOA13. The second reason is the underestimated surface cooling over the continental shelf that leads to a reduced AABW formation in the model and therefore to a reduced subduction of the surface freshwater (section 3.7). Thirdly, an overly-stable surface layer or too little surface mixing also contributes to a lack of subduction of

freshwater in this region, making the surface ocean fresher and the deep ocean saltier. At the end of the spin-up the surface salinity drift is small (note the different scales) and depends on the region, indicating that the model's surface is largely equilibrated and most of the trends result from internal variability. In the subsurface ocean a prevailing salinification of the AAIW and SAMW is the most prominent feature (see section 3.7 for more details).

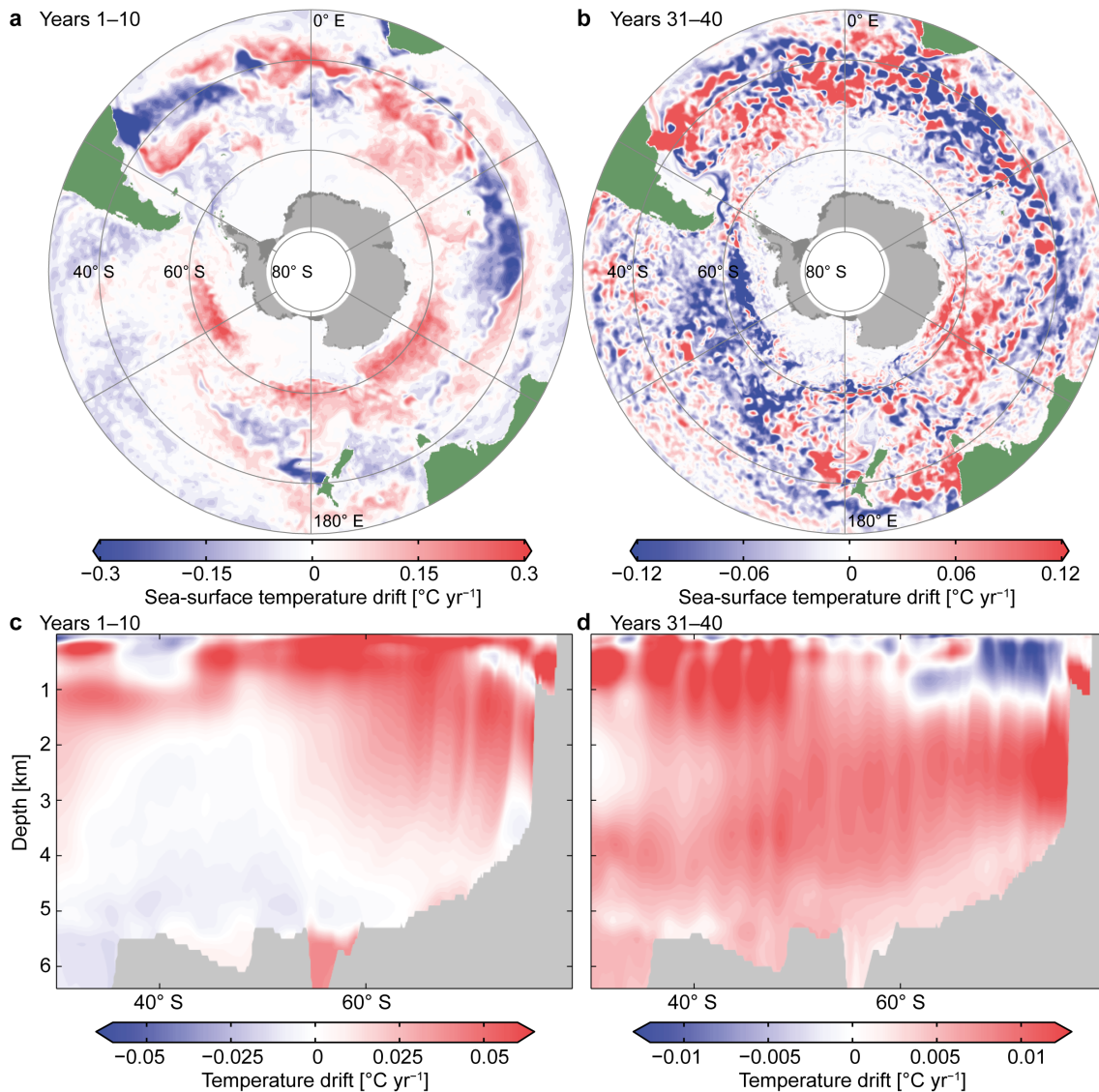


**Figure 3.7 Temperature drift during spin-up simulation:** Sea-surface temperature during simulation years 1 to 10 (a) and 31 to 40 (b). Cross-sections showing the zonal mean subsurface temperature drift during simulation years 1 to 10 (c) and 31 to 40 (d). Note the different scales.

The surface temperature drift shows a warming of high latitudes and a weak cooling of lower latitudes in the beginning of the simulation (Figures 3.7 a–b). At the end of the spin-up simulation, most of this surface temperature drift disappeared. A more critical feature is a broad-scale subsurface warming (Figures 3.7 c–d), which, even though at a much smaller rate, still persists at the end of the spin-up. This subsurface temperature drift can probably be attributed to a too stable surface layer and too little surface heat loss. As the Southern Ocean gains heat through the inflow of relatively warm NADW through the northern boundary, it needs to lose this heat to the

atmosphere at the high-latitude surface ocean or the outflow of surface waters, SAMW, or AAIW. If this heat loss does not equal the inflow at the northern boundary the model temperature will continue to drift in the subsurface. Future efforts should be devoted to resolving this issue.

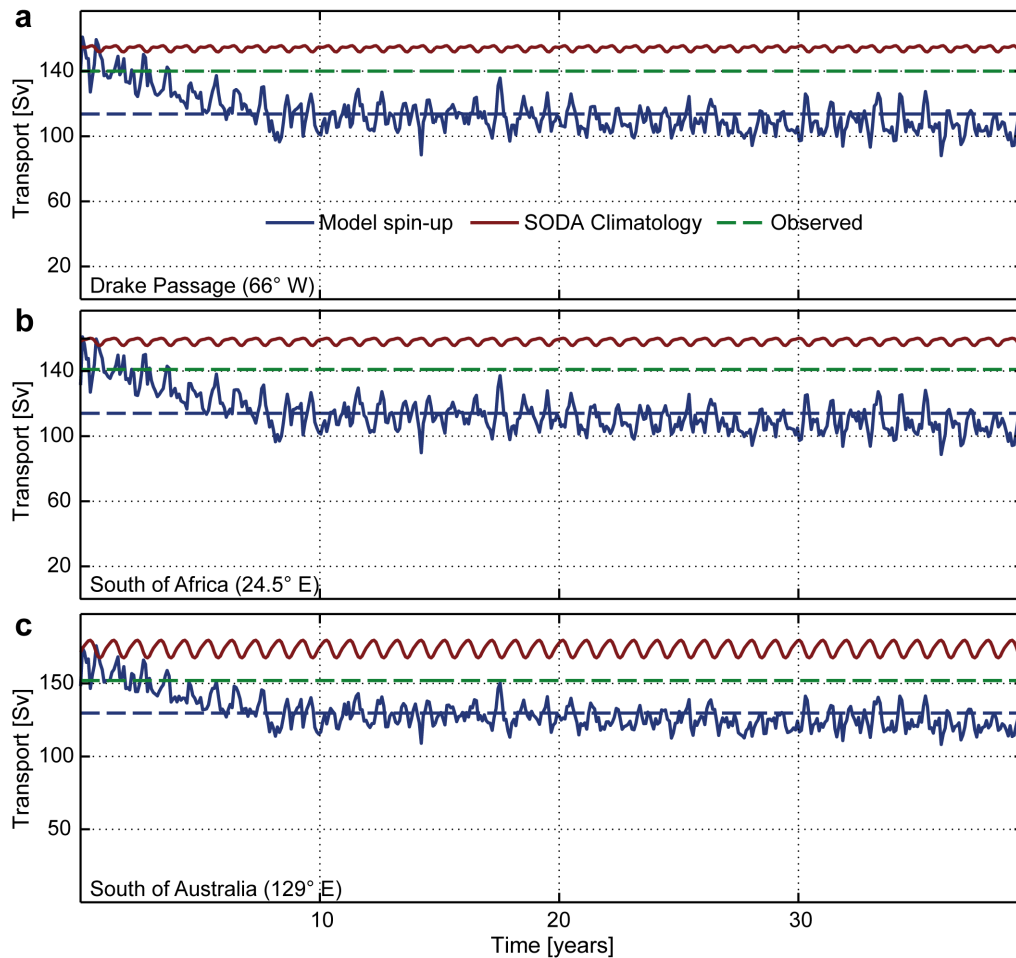


**Figure 3.8 Transport drift during spin-up simulation:** Time series of vertically integrated zonal volume transport (Sv) through (a) Drake Passage, (b) south of Africa, and (c) south of Australia. The blue curve shows the model spin-up simulation and the blue dashed line the respective mean, the red curve the SODA climatology that was used to force the model at the northern boundary (section 3.5.5, and the green dashed line shows the approximate mean values from observations (Ganachaud and Wunsch, 2000; Naveira Garabato et al., 2014; Koenig et al., 2014).

Figure 3.8 shows the temporal evolution of the vertically integrated zonal volume transport in the model with the ACC through Drake Passage, south of Africa, and south of Australia. Due to the fixation of the northern boundary (section 3.5.5), the relative transport ratio between these gateways does not change but its absolute magnitude changes over time depending on the surface forcing and the meridional density gradient. The transport decreases by about 30 Sv over the first 10 years and only slightly thereafter. A more detailed evaluation of the transport is provided in section 3.7. To account for any remaining model drift in each of the experiments, I ran an additional control simulation that is used to subtract the model drift from the experiments presented in chapters 4 and 5.

## 3.7 Model evaluation

In this section, I only evaluate the model physics of the  $0.25^\circ$  resolution model, because the ocean circulation model was the key focus of this chapter. A brief evaluation of the biogeochemical model is provided in chapter 5. The evaluation is based on the last 10 years of the climatological mean spin-up simulation (section 3.6), i.e., simulation years 31 to 40, when the model drift is comparably small.

### 3.7.1 Circulation

In section 3.5.5, I introduced a new concept for the northern boundary in ROMS, where the vertically integrated transport is fixed to the boundary condition in the Pacific and Indian Ocean sectors and is free to adjust in the Atlantic sector. Figure 3.9 shows this vertically integrated transport at the northern boundary compared to the SODA boundary forcing. The overall net transport through the boundary is zero, because the northern boundary is the only open boundary in the domain. Starting at the African continent and going eastward, the cumulative transport in the Indian Ocean amounts to  $-16$  Sv, which agrees with the estimate by Ganachaud and Wunsch (2000) and is a slightly higher southward transport than the estimated  $-11$  Sv by Sloyan and Rintoul (2001a), Stammer et al. (2003), or Talley (2003) for the Indian Ocean. In the model and in SODA,  $-20$  Sv are transported through the Mozambique Channel and  $+4$  are transported northward east of Madagascar. The former is a slightly higher southward transport than the estimated  $-17$  Sv by Ridderinkhof et al. (2010). In the Pacific,  $+16$  Sv are transported to the north by the model and SODA, which is again in good agreement with the estimate by Ganachaud and Wunsch (2000) and slightly higher than the one by Stammer et al. (2003) and Naveira Garabato

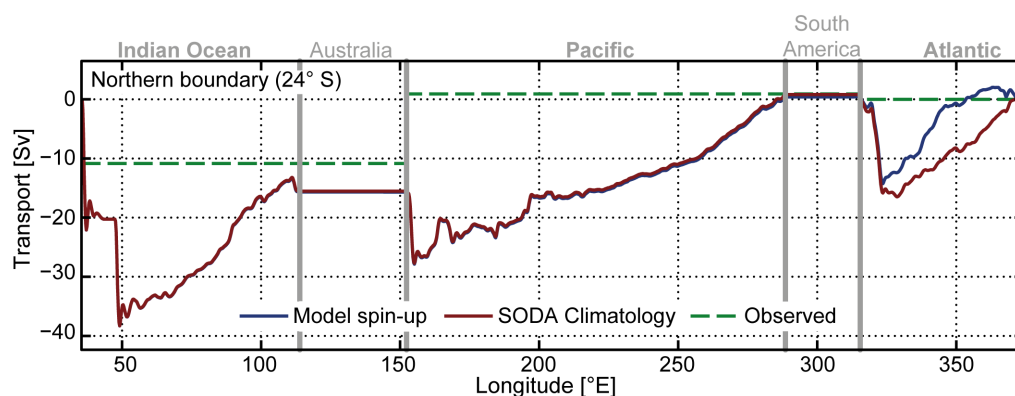


**Figure 3.9 Meridional transport at the northern boundary:** Cumulative, vertically integrated meridional volume transport (Sv) through the northern boundary. The blue curve shows the model simulation, the red curve the SODA climatology that was used to force the model at the northern boundary (section 3.5.5), and the green dashed line shows the approximate mean from observations for each basin, which has to sum up to zero over the entire northern boundary (Ganachaud and Wunsch, 2000; Stammer et al., 2003; Naveira Garabato et al., 2014). Gray bars denote continental margins.

et al. (2014). In the Atlantic, where the model can adjust the boundary transport, a slightly too weak southward transport occurs with the western boundary current. This lack of transport into the domain is compensated by a slightly too weak northward Sverdrup transport in the central and eastern Atlantic subtropical gyre. The overall transport in the Atlantic in the model amounts to  $-0.4$  Sv, similar the observed values between 0 and  $-1$  Sv (Ganachaud and Wunsch, 2000; Naveira Garabato et al., 2014), which should roughly equal the flow through Bering Strait.

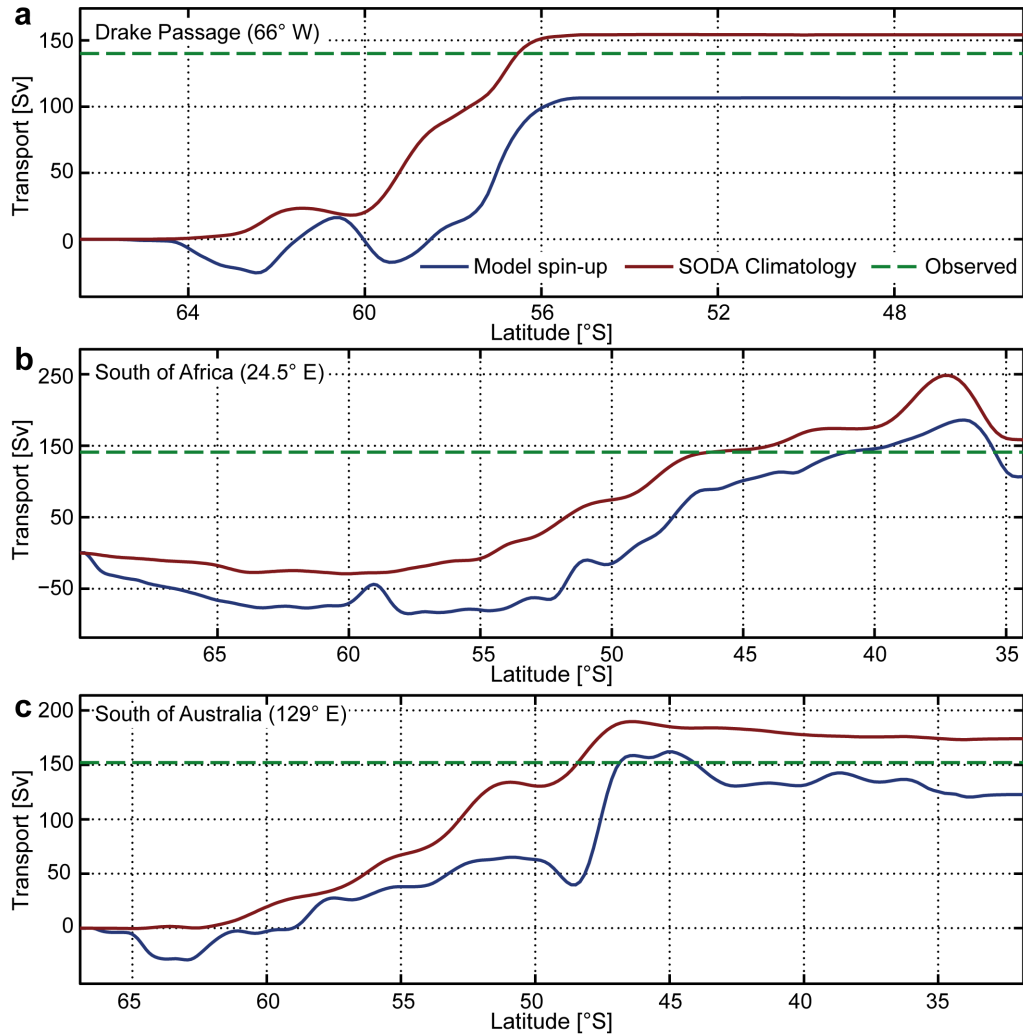


**Figure 3.10 Zonal transport between ocean basins:** Cumulative, vertically integrated zonal volume transport (Sv) through (a) Drake Passage, (b) south of Africa, and (c) south of Australia. The blue curve shows the model simulation, the red curve the SODA climatology that was used to force the model at the northern boundary (section 3.5.5), and the green dashed line shows the approximate overall mean from observations (Ganachaud and Wunsch, 2000; Naveira Garabato et al., 2014; Koenig et al., 2014).

Between the ocean basins there is a westward transport close the Antarctic continent with the coastal current and a much stronger eastward transport with the ACC further north as illustrated by the cumulative transport shown in Figure 3.10 for each of the three major gateways. In the model, these transports amount to  $+103$  Sv through Drake Passage,  $+104$  Sv south of Africa, and  $+119$  Sv south of Australia. While the relative ratio between these transports is set through the northern boundary forcing and therefore agrees well with observations, their absolute eastward

transport is about 37 Sv lower than the observation based estimates (Ganachaud and Wunsch, 2000; Naveira Garabato et al., 2014; Koenig et al., 2014). This bias is related to a too small north—south density gradient in the model, which is typical for an overly-stable high-latitude surface ocean. In contrast, test experiments showed that the occurrence of high-latitude open-ocean deep convection would lead to an overestimation of the ACC transport, in agreement with the findings by Stössel et al. (2015). The transport shows a realistic meridional structure with two to three jets in the ACC region that are associated with the main fronts (Cunningham et al.,

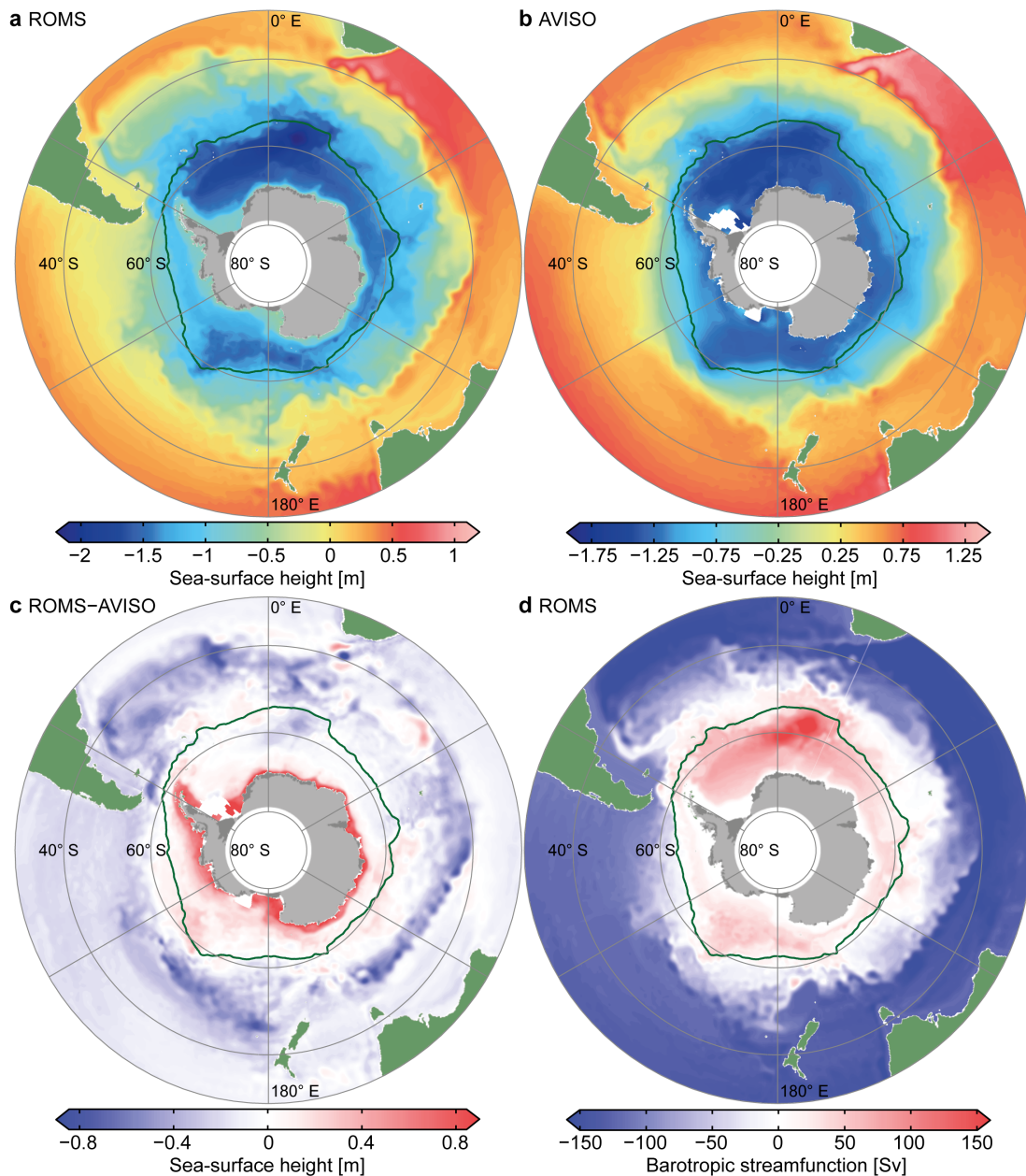


**Figure 3.11 Sea-surface height and barotropic streamfunction showing the horizontal circulation:** Sea-surface height from the model (a) and AVISO satellite product (b). The satellite product is produced by Ssalto/Duacs and distributed by AVISO with support from Cnes, <http://www.aviso.altimetry.fr/duacs>. Note the different color scale to adjust for the difference in mean sea level between the two estimates. (c) The sea-surface height difference between the model and the satellite data adjusted whereas the mean difference has been removed. (d) Barotropic streamfunction from the model. Green contour line: climatological mean sea-ice edge.

2003). These jets are somewhat stronger than those by the coarser resolution SODA simulations. The westward coastal transport amounts to about  $-30$  in most of the Indian Ocean and Pacific sectors, in agreement with the estimates by Peña-Molino et al. (2016). In the Atlantic sector, the transport is about  $-25$  Sv in the vicinity of the Antarctic Slope Front, which is considerably higher than the estimate of about  $-10$  Sv by Dong et al. (2016). The overall westward transport associated with the southern part of the Weddell Gyre (Figure 3.10b) amounts to about  $-70$  Sv, which is comparable to the estimate by Schröder and Fahrbach (1999). In summary, the westward coastal transport is slightly overestimated due to a too strong meridional density gradient and the eastward ACC transport slightly underestimated due to a too weak meridional density gradient.

The simulated horizontal circulation pattern agrees generally well with the observed structure (Figure 3.11), which can be depicted from the comparison of the sea-surface height patterns in the model with the observed pattern from satellite data (AVISO; produced by Ssalto/Duacs and distributed by AVISO with support from Cnes, <http://www.aviso.altimetry.fr/duacs>). It shows strong gradients in the ACC region with several typical meridional excursions associated with topographic features. Overall, the meridional gradient is slightly too weak, confirming the previously stated underestimation of the ACC strength. On the Antarctic continental shelf, the sea-surface height is significantly overestimated in the model due to a too low density of the continental shelf waters. The stronger Weddell Gyre and the weaker Ross Gyre are clearly visible in the sea-surface height field and the barotropic stream-function of the model, which is the total transport integrated from the Antarctic continent towards the north (see e.g. Zika et al., 2012).

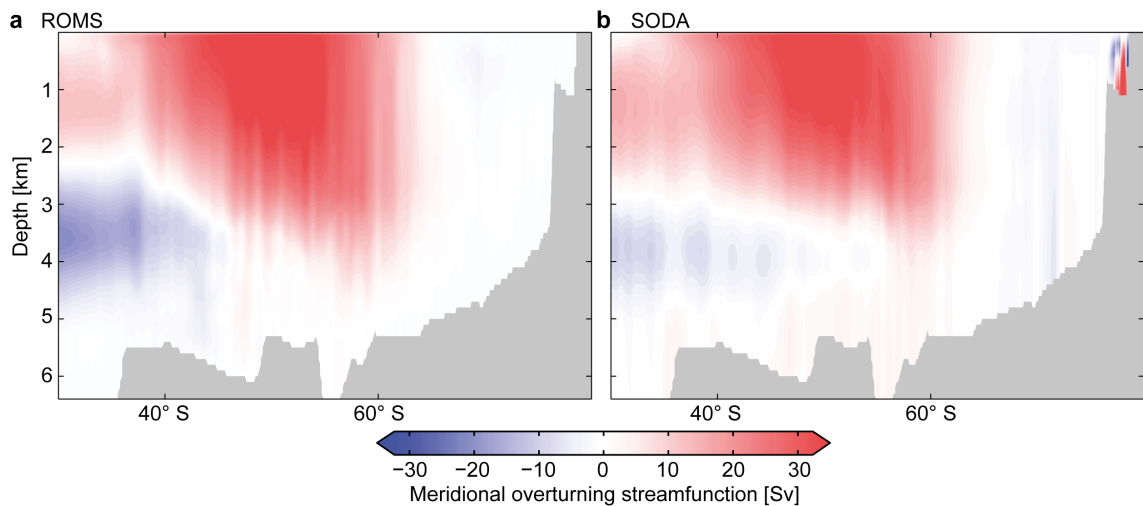


**Figure 3.12 Meridional overturning circulation:** Zonally averaged meridional overturning stream-function calculated from ROMS (a) and SODA (b).

In the vertical, the meridional overturning circulation (Figure 3.12) shows a clear upper and lower circulation cell in the model. This circulation looks very similar to the one in SODA, which is used to force the model at the northern boundary. However, it should be noted that the model's ocean interior runs freely, i.e., it is not adjusted to the SODA circulation. Nevertheless, it remains unclear how much of the overturning circulation in the model is governed by the northern

boundary forcing. Compared to the estimates by e.g. Lumpkin and Speer (2007) or Marshall and Speer (2012), the upper circulation cell seems too strong and the lower circulation cell too weak. Certainly, some of the biases in the model's water-mass structure (see below) might result from a dependence of the overturning circulation on the northern boundary and a replacement of the northern boundary transport by alternative products might improve the circulation.

### 3.7.2 Surface processes

In this section, I will evaluate the ocean's surface processes based on a comparison of sea-surface salinity (Figure 3.13), sea-surface temperature (Figure 3.14), and surface mixed layer depth (Figure 3.15) to observational data products. The latter products comprise the annual mean Argo-only climatology of CARS2009 (developed by CSIRO; Dunn and Ridgway, 2002; Ridgway et al., 2002), and the EN4 Objective analyses derived from quality controlled ocean profile data (version 4.2.0; 1979–2014; Ingleby and Huddleston, 2007; Good et al., 2013), and a combined Argo and CTD profile derived mixed layer depth product (de Boyer Montégut et al., 2004). For this comparison, the mixed layer depth from ROMS has been re-computed using the same density criterion as the observational product, because the mixing depth computed by ROMS itself uses a different criterion (for details see Eberenz, 2015).

The model suffers from a too fresh surface ocean in the sea-ice region, most of the South Atlantic, and, more extremely, over the Antarctic continental shelf (Figure 3.13). This signal becomes even more apparent during austral summer. A potential explanation for this fresh bias at the surface is provided by the too shallow mixed layer in the sea-ice region mostly during summer but also during winter (Figure 3.15). North of the sea-ice edge, a positive salinity bias exists in the Pacific and Indian Ocean sectors. A potential explanation for this bias is a reduced horizontal mixing of the water masses in the not fully eddy-resolving  $0.25^\circ$  model.

The sea-surface temperature shows a slight warm bias in the high-latitude surface ocean—mostly around the sea-ice edge (Figure 3.14). This warm bias originates from the austral summer period and is most likely related to an overly-weak summer-time mixing. Even though the modification of the mixing processes in KPP (section 3.2.2) that I introduced to ROMS greatly helped to reduce some of these biases, the model still has problems to accurately simulate mixing processes during the strongly stabilizing melting conditions during summer. Besides the shallow bias of the surface mixed layer in high latitudes during summer, a too deep mixed layer occurs north of the frontal region and downstream of Drake Passage during austral winter (Figure 3.15). Nevertheless, the model is generally able to simulate the spatial and temporal evolution and characteristic patterns of the surface mixed layer depth in the Southern Ocean (de Boyer Montégut et al., 2004) with deep winter-time mixed layers north of the frontal region during winter and a more annular and somewhat shallower mixed layer in the ACC region during summer.

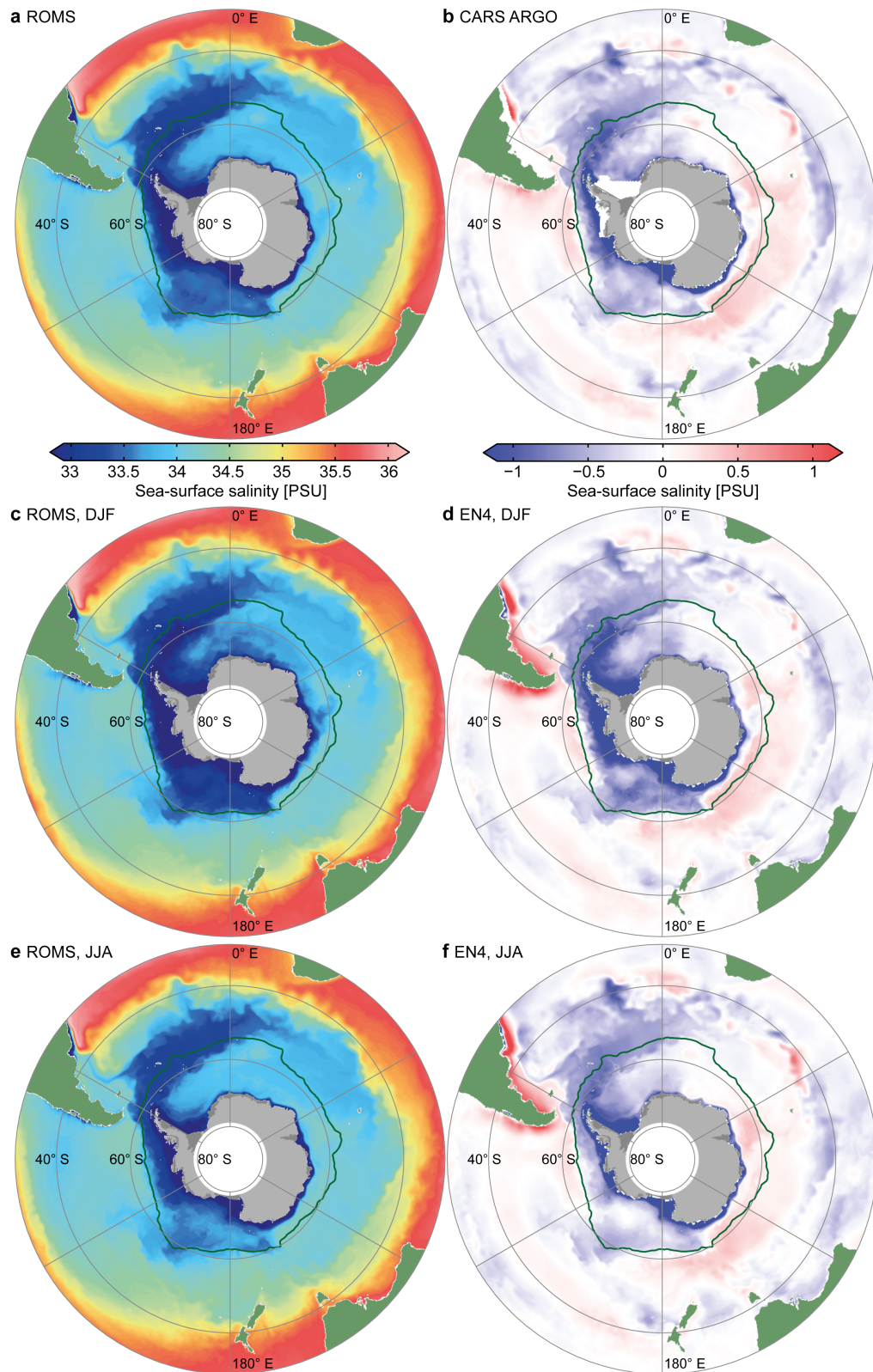


**Figure 3.13 Sea-surface salinity:** Annual mean sea-surface salinity in ROMS (**a**) and its difference to the Argo-only climatology of CARS2009 (**b**). Austral summer (DJF) mean sea-surface salinity in ROMS (**c**) and its respective difference to the EN4 climatology (**d**). (**e**) and (**f**) as (**c**) and (**d**) but for austral winter (JJA). The green contour line denotes the climatological mean sea-ice edge.

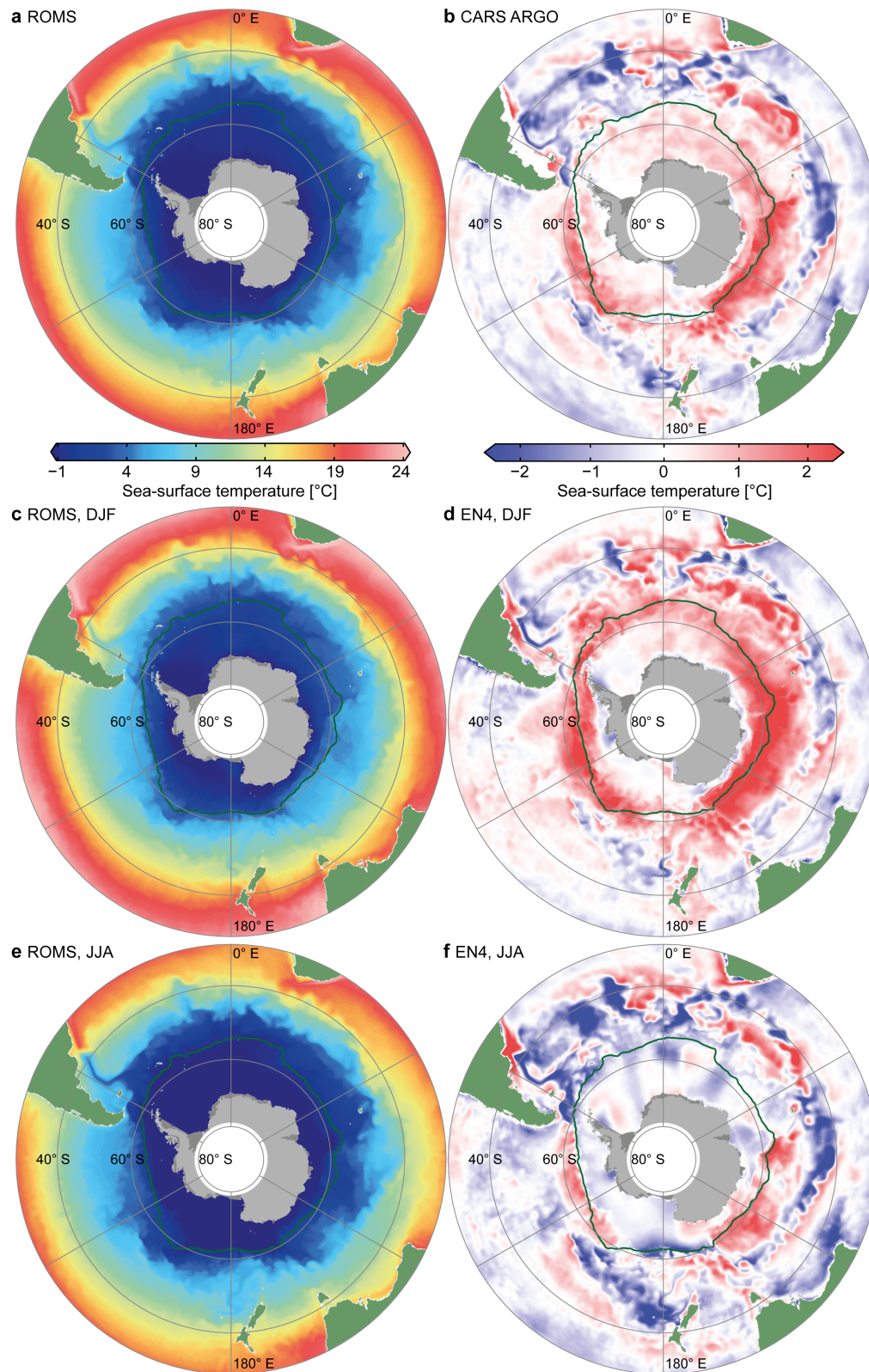


**Figure 3.14 Sea-surface temperature:** Annual mean sea-surface temperature in ROMS (a) and its difference to the Argo-only climatology of CARS2009 (b). Austral summer (DJF) mean sea-surface temperature in ROMS (c) and its respective difference to the EN4 climatology (d). (e) and (f) as (c) and (d) but for austral winter (JJA). The green contour line denotes the climatological mean sea-ice edge.

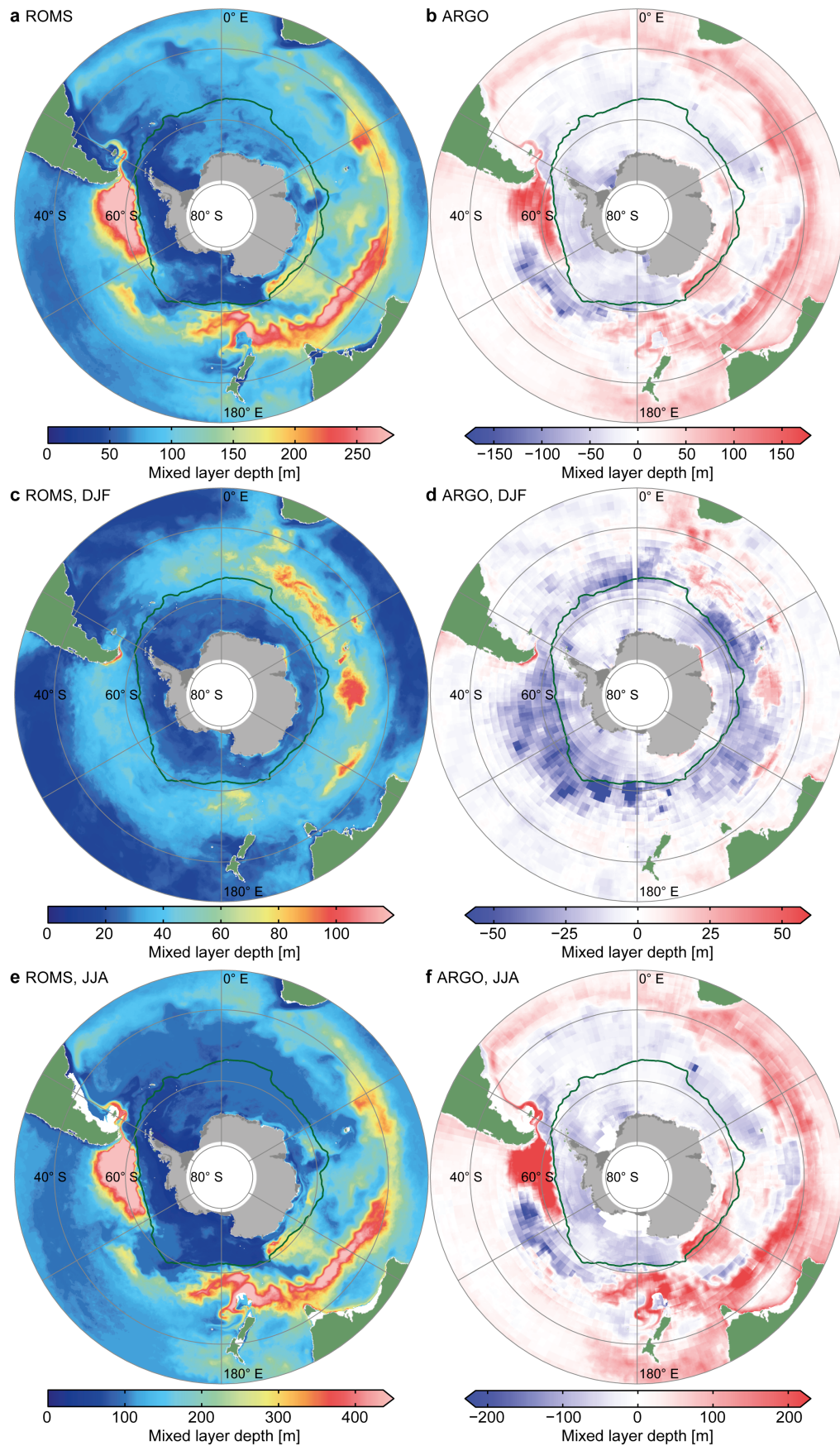


**Figure 3.15 Surface mixed layer depth:** Annual mean surface mixed layer depth computed from ROMS (a) and its difference to an Argo-derived product (b). (c) and (d), and (e) and (f) as (a) and (b) but for austral summer (DJF) and austral winter (JJA), respectively. The green contour line denotes the climatological mean sea-ice edge. Note the different scales. See text for details.

### 3.7.3 Hydrography & water masses

The most challenging comparison for an ocean circulation model of the Southern Ocean is the difference between the model's temperature and salinity and observational data in the vertical. Figure 3.16 shows these zonal mean fields compared to the WOA13 database (Boyer et al., 2013; Locarnini et al., 2013; Zweng et al., 2013). Overall, ROMS is able to represent the Southern Ocean water mass structure with a fresh and cold surface layer, a warm and salty deep water layer, and a cold bottom water layer. However, the latter layer is most likely not yet fully equilibrated by the end of the spin-up simulation. Close to the surface, the model is also able to represent the cold and relatively fresh subsurface winter-water layer with an even fresher and warmer summer-water layer on top (not shown). In lower latitudes the characteristic fresh AAIW and SAMW layer is visible in the model.

Despite this general ability of the model to represent the ocean water masses, major biases exist. Among these biases is a pronounced positive salinity bias in the region of the AAIW and SAMW, which are too shallow, too warm, and too salty in the model. These issues are

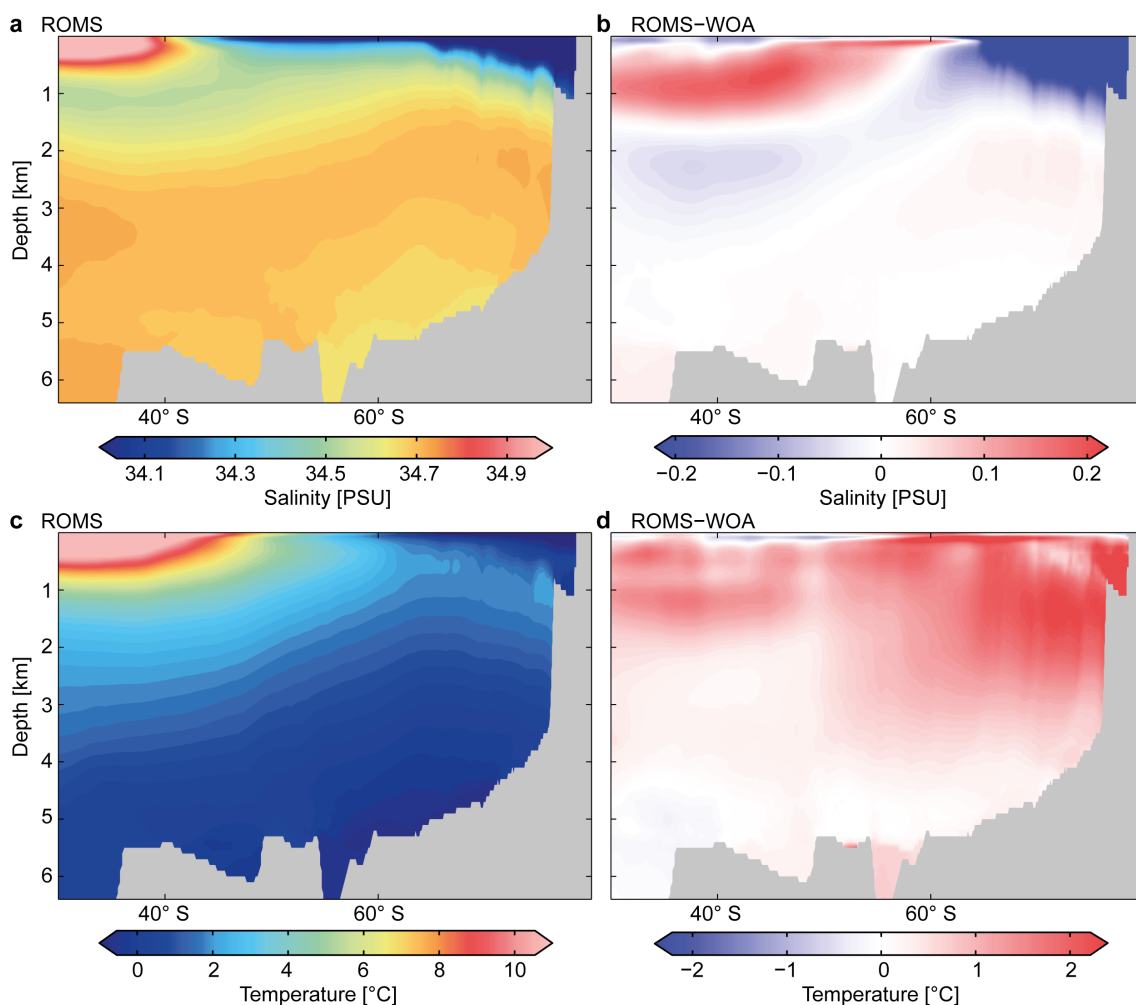


**Figure 3.16 Zonal mean temperature and salinity:** Annual, zonal mean temperature and salinity fields from ROMS (a) (b) (c) (d).

mostly related to the fresh biases at the high-latitude ocean surface, because too little freshwater is transported northward and mixed into the subsurface layers where it would be transported with AAIW and SAMW. An additional degradation of AAIW and SAMW might occur due to spurious diapycnal mixing in the ocean interior (section 3.1.1). A second major bias is the too fresh Antarctic continental shelf that I already noted when describing the surface salinity biases. This problem is directly related to a considerable subsurface warm bias in the high-latitude Southern Ocean. On the one hand, the too fresh surface ocean reduces the subduction of cold AABW, which leads to a subsurface warming. On the other hand, the too fresh surface ocean might also be related to a too weak surface heat loss in the coastal ocean that prevents the subduction of these water to the subsurface. This latter process becomes apparent as a slightly too salty deep ocean. Even though there is a large uncertainty in the total amount of AABW production and the strength of the lower circulation cell (about 30 Sv, see section 1.3.1), with only about 10 Sv of northward transport in the AABW layer, the model seems to have a too weak AABW production. In summary, most of the problems in the model's hydrography seem to result from an unrealistically weak vertical exchange.

### 3.8 Summary of model developments & future directions

In this chapter, I presented a new regional model for the Southern Ocean. The underlying physical ocean circulation model is a regional configuration of ROMS (Shchepetkin and McWilliams, 2003, 2005, 2009a), which has a stretched, terrain-following vertical coordinate system. A key challenge with models that have such a coordinate system is the occurrence of spurious diapycnal mixing in the deep ocean where isopycnals cross the vertical coordinates. This process leads to a long-term degradation of interior ocean water masses in basin-scale applications if the model is running freely, i.e., without restoring. I mitigated the problem in several ways: (1) Spurious diapycnal mixing is reduced through increasing the vertical and horizontal resolution; (2) a careful choice of the vertical stretching parameters leads to a damping of terrain-effects in the upper ocean and reduces the degradation of AAIW and SAMW; (3) an enhanced smoothing of the topography reduces terrain-effects throughout the water column and improves the representation of all water masses. I counteracted the reduction in bottom roughness induced by (3) by increasing the bottom roughness length scale in the mixing scheme to slow down unrealistically strong coastal currents. An important future development to further reduce these effects would be the implementation of an isoneutral advection scheme (Lemarié et al., 2012b).

To obtain a realistic mean ocean circulation, I modified the implementation of the northern boundary condition. Using a specified boundary condition for the barotropic mode that directly sets the outermost grid cell to the vertically integrated transport of the lateral forcing in the Pacific and Indian Ocean sectors, constrains the relative exchange of water masses between the basins. Without this constraint the model would drift due to an unknown water mass exchange north of the northern boundary. In order to reduce the effect of barotropic waves that might get trapped in the domain due to this fix, I added a sponge layer with enhanced viscosity along the northern boundary and used a radiation boundary condition in the Atlantic basin only. The latter enables the model to still adjust its mean circulation to the forcing. Moreover, the location of the northern boundary at a latitude where the transport is mostly perpendicular to the boundary helped to reduce boundary artifacts and increased the stability of the model. Another important change to obtain a realistic circulation around the southern boundary—the Antarctic continent—is the use of RTopo-1 (Timmermann et al., 2010) for the bathymetry, and land and ice-shelf masks. Finally, the refinement of the horizontal resolution towards the south, enables the model to better represent the ACC and coastal circulation around Antarctica at low computational cost. Moreover, this horizontal grid naturally follows the decreasing baroclinic Rossby deformation radius towards the south and therefore helps the model to resolve baroclinic instabilities. While I only use the  $0.5^\circ$  and  $0.25^\circ$  configurations of the model in this thesis, a fully eddy-resolving resolution of  $0.1^\circ$  will further improve the circulation and lateral mixing processes in future.

Vertical mixing processes in ROMS are parameterized through a first-order closure scheme (KPP; Large et al., 1994; McWilliams et al., 2009). This common mixing scheme tends to produce

a too shallow mixed layer in the Southern Ocean surface waters in summer, which led to too salty AAIW and SAMW and, in extreme cases, spurious deep ocean convection in the high-latitudes in winter. I found that this bias is induced by two problems. Firstly, the shallow mixed layer was not represented well when the vertical resolution was insufficient and the diffusivity dropped to a background value. The use of 64 vertical layers can mostly avoid such an effect. Additionally, I implemented an option that calculates the vertical diffusivity for the first layer interface based on the surface forcing if the mixed layer shoals below this level. The second issue is a very fast stabilization and a related decrease of the mixed layer depth during summer after strong mixing events, which occurs due to the strongly stabilizing buoyancy forcing. Consistent with Timmermann and Beckmann (2004) and Dinniman et al. (2003), I found that a formulation of the mixed layer depth as suggested by Lemke (1987) and Markus (1999) that solely depends on the surface forcing and an exponential dissipation function provides much more realistic results for the mixed layer depth decay under such strongly stabilizing conditions. This implementation resulted in the largest improvement. In future, the implementation of a damping function that accounts for the dissipation of inertial shear after the passage of a storm or eddy under strongly stabilizing conditions would be desirable. Additionally, the use of a higher maximum diffusivity for the calculation of the mixing induced by shear and stability improved the mixing processes just below the mixed layer and spared the need for an additional convective adjustment formulation.

The model is forced with momentum, heat, and freshwater fluxes from the atmosphere, sea ice, and land ice. I made multiple modifications to the surface forcing creation tools in ROMS. Among these changes are an improved interpolation scheme, more suitable and consistent fields for the surface temperature and salinity restoring, a correction of the fluxes in the presence of sea ice, an addition of sea-ice melting and freezing fluxes, an addition of river input, and an addition of iceberg melting fluxes. Moreover, I implemented the possibility to add interior ocean sources of freshwater, heat, and tracers to add subsurface fluxes of ice-shelf melting. I added multiple options to treat the presence of sea ice in the model. Among these are a calculation of heat fluxes under ice, and a parameterization of convective brine plumes. I also added an option to perform only a partial surface restoring to temperature and salinity whenever reliable data is available. All these changes related to the surface forcing led to major improvements and a reduction of biases. One of the key remaining biases in the forcing data is a warm bias in the ERA-Interim surface heat flux, and a bias correction might result in further improvements.

While the above described changes to the model result in a general ability to represent the water-mass structure, circulation, and mixing processes in the Southern Ocean, several pronounced model biases and challenges remain for the future. The most problematic biases are a too fresh coastal ocean, too little AABW formation, a warm bias at the subsurface, a surface fresh bias in the sea-ice region and the South Atlantic, and a too shallow, warm, and salty AAIW and SAMW. Many of these biases are probably directly related. The circulation of the model is generally very well represented and biases are most likely related to either the surface heat flux or mixing processes. Especially, forcing the model with a mostly fixed surface heat flux seems prob-

lematic as the model builds up heat in the ocean interior that cannot be lost to the high-latitude atmosphere as long as the heat flux is prescribed. The implementation of a bulk formulation for the surface heat flux might help to mitigate this problem. In addition to the suggested future improvements above, an update of the equation of state to its newest version (TEOS-10), an implementation of surface mixing by waves, and a tidal model might help to reduce the remaining biases. Moreover, a completion of the partly implemented sea-ice model and an ice-shelf cavity model might be useful to study feedbacks between the ocean and the ice in future. Together with the sea-ice model a representation of sea-ice biogeochemistry and the input of nutrients associated with glacial discharge might also be desirable to better understand the biological production, the ecosystem, and the carbon fluxes in the high latitudes.

**Acknowledgments:** I would like to thank Matthias Münnich for his contributions to the model development presented in this chapter. I am thankful to Ivy Frenger for providing an initial basis of the Southern Ocean ROMS setup. I thank Samuel Eberenz for his help in evaluating this model and developing analysis tools. I am thankful to Alexander F. Shchepetkin for sharing his latest ROMS developments with us. I thank Julien Le Sommer for sharing his experience in modeling the Southern Ocean in a regional configuration and providing valuable suggestions to solve some of the issues presented in this chapter. I also thank Michael Dinniman for a valuable discussion on the surface mixing scheme in the model. This work was supported by ETH Research Grant CH2-01 11-1.